LUDWIG MAXIMILIAN
UNIVERSITY OF MUNICH

FACULTY OF PHYSICS

METEOROLOGICAL INSTITUTE

Master's Thesis

Tropical Waves and Predictability in Simulations with a Stochastic Convection Scheme

Author:	Tatsiana Bardachova
Supervisor:	Prof. Dr. George Craig
Advisor:	Dr. Tobias Selz
Submission date:	22. June 2022

LUDWIG-MAXIMILIANS-
UNIVERSITÄT
MÜNCHEN

FAKULTÄT FÜR PHYSIK

METEOROLOGISCHES INSTITUT

Masterarbeit

Tropische Wellen und Vorhersagbarkeit in Simulationen mit stochastischem Konvektionsschema

Verfasser:	Tatsiana Bardachova
Betreuer:	Prof. Dr. George Craig
Berater:	Dr. Tobias Selz
Abgabe:	22. Juni 2022

Abstract

The current study investigates the representation of tropical waves and estimates tropical predictability limits in numerical simulations with the stochastic convection scheme. The study of predictability limits included the investigation of the current practical predictability limit, intrinsic predictability limit and transition between them. For these purposes, the global numerical simulations on the base of ICOsahedral Non-hydrostatic Model including the Plant-Craig stochastic convection scheme were applied with, rescaled in several steps, the current estimates of initial condition uncertainty of 12 real cases. The obtained estimation of intrinsic predictability limit in the tropics exceeds two weeks and is longer than the estimation for the mid-latitudes, especially for large scales. Also, the shallower slope of background kinetic energy comparing to the mid-latitudes has been estimated. Based on the simple Lilly model, it was found that shallower spectral slope provide longer predictability limits and can be a potential source of longer tropical predictability. The identification of tropical waves showed very weak wave signals in the total precipitation rate and outgoing longwave radiation fields, however Kelvin waves, $n = 0$ equatorial-Rossby waves and mixed Rossby-gravity waves were recognized. The stronger signals of these waves were observed in wind divergence field. Due to weak wave signals and slightly coupling to convection, the misrepresentation of the tropical waves in numerical simulation with the stochastic scheme was concluded and prevent to make a conclusion about tropical waves as a source of longer tropical predictability limits.

Contents

Chapter 1

Introduction

In recent decades, weather forecast quality has been significantly improved by developing observational techniques, new data assimilation procedures and numerical modeling. Leading position in global modeling is occupied by ECMWF, with the ensemble lead time ahead by about one day compared to other global centers and with a predictability time limit of about one week (ECMWF 2018). At the same time, the predictability time limit may vary across geographical zones for many reasons: due to regional climatic differences, due to inhomogeneities in climate datasets and their impact on uncertainties in the initial conditions, and due to the different accuracy of data assimilation techniques for different regions.

With respect to climate, the atmosphere is divided into broad latitude zones in which the flow pattern is governed by certain underlying dynamics. For instance, extratropical flow pattern is characterized by strong pressure and temperature gradients and, consequently, by the predominance of baroclinic disturbances. Tropical flow pattern has much weaker pressure and temperature gradients as well as zones of high humidity, therefore tropical flow pattern is driven primarily by moist convection. As a result, climatological differences between zones may change predictability time limit of the particular meteorological variable. For instance: clouds and rains may have more spontaneous behavior and therefore have shorter predictability time limits in the tropics than at higher latitudes, and the opposite is true for temperature (Sobel 2012). Also, because current global numerical weather prediction (NWP) models cannot properly resolve moist convection, they employ different parameterizations, which significantly affects the forecast errors, especially in the tropics, since convective processes predominate in this region. Additionally, weather prediction in the tropics becomes challenging also due to an insufficient observational network and data assimilation techniques optimized for mid-latitude conditions, which affect the accuracy of the initial conditions (Vogel et al. 2020). The combination of the factors described above leads to a relatively low forecast skill for the tropical region. However, Zhu et al. (2014), exploring the forecast skill for precipitation of a global coupled ocean–atmosphere model over a range of time scales, showed that tropical forecast skill is low only at lead times from one day to a week. They found that the forecast accuracy near the equator becomes equal to or greater than that in any other ranges of latitudes at about 4 days in December-February and 1 week in June-August, and then remains

better than the extratropical forecast accuracy.

Besides the practical predictability time limit, conditioned by the current forecast skill, there is an intrinsic limit of atmospheric predictability (Lorenz 1969), what is the limit to which the predictability time can be improved under the nearly perfect initial conditions and dynamical system representation. The existence of the finite intrinsic limit is caused by the chaotic nature of the atmosphere and arises from scale interaction and rapid error growth in a multiscale flow. According to many studies, for the mid-latitudes, the intrinsic limit of predictability has an estimated value about two weeks (Zhang et al. 2019; Judt 2020; Selz et al. 2022). At the same time, it has been shown that estimations of the intrinsic predictability time limit in the tropics are more than two weeks, which is systematically longer than for the mid-latitudes, and this feature is especially noticeable at large scales (Ying and Zhang 2017; Judt 2020). Thus, although the current weather prediction skills for the tropics appear to be more challenging compared to the mid-latitudes, the potential improvement in predictability times in the tropics is greater. However, the reasons for the longer intrinsic predictability time limits in the tropics are still unclear.

Several recent studies investigating tropical predictability time limits have focused their attention on large-scale convectively coupled equatorial waves (CCEWs) and intraseasonal oscillations such as the Madden–Julian oscillation (MJO) because of their relatively long predictability (Ying and Zhang 2017; Li and Stechmann 2020; Judt 2020). CCEWs seem to be more resistant to error growth than baroclinic systems and therefore were proposed as a possible source of longer tropical predictability. However, the predictability of equatorial waves and their contribution to the predictability in the tropics are still poorly understood. The point is that employing of the convection parameterization schemes leads to a misrepresentation of the equatorial waves (Judt and Rios-Berrios 2021), which makes the estimations of the predictability time limit values untenable. High resolution models are capable to resolve convection processes for a correct assessment of the predictability time limits, but it is a very computationally expensive way. Recently Judt (2020) has performed an identical-twin predictability experiment, able to simulate convective processes, aiming to estimate the predictability time limits for the different equatorial wave types, but only two simulations have been investigated. Additionally, Judt has concluded that the spectral slope of the background kinetic energy is latitude-dependent and thus can be specified by the underlying dynamics, and spectral slope estimation for the tropics is shallower than for the extratropics. He obtained the quasi-uniformal spectral slope close to -5/3 in the tropics, the slope near -3 at the synoptic scales and near -5/3 at the mesoscales in the mid-latitudes and the slope close to -3 for the polar regions. Rotunno and Snyder (2008), generalizing the Lorenz model for the predictability of a flow with many scales of motion (Lorenz 1969), showed that the spectral slope of the background kinetic energy of the flow plays a much more significant role in the error-energy evolution than the dynamics governing the error growth. The obtained results are consistent with the Lilly's (1972) simple scaling arguments for the predictability loss considering only the kinetic energy spectrum. Based on this results, it may be assumed that the variations in spectral slopes between different regions may be an additional source of longer predictability time limit

in the tropics.

The assessment of the intrinsic predictability time limit requires a perfect model assumption, thus a convection-permitting model resolution, since it may be significantly affected by simulation of the convective processes. Comparison between the upscale error growth simulated on the convection-permitting grid with error growth simulated on coarser grids both with the deterministic and stochastic convection schemes showed, that the error growth due to convection is underestimated for simulations with parameterized convection for the grid resolutions $\geq$ 5 km (Selz and Craig, 2015a). However, the stochastic convection scheme is able to better reproduce the convection-permitting results due to taking into account the missing variability near the grid scale. Since the conduction of numerical simulations with a convection-permitting resolution is very computationally expensive, the employing of the stochastic convection scheme may compensate slow upscale error growth due to convection at lower resolutions, and thus better represents the perfect model assumption. However, the representation of equatorial waves in numerical simulations with the stochastic convection scheme has not yet been evaluated.

The present study is devoted to estimating the limits of predictability for the tropics and considering possible sources of longer tropical intrinsic predictability, i.e. equatorial waves and nature of the slope of the background kinetic energy spectrum. For the study, the numerical simulations by ICOsahedral Non-hydrostatic (ICON) Model with the stochastic convection scheme have been taken, conducted by Selz et al. (2022) to investigate the transition from practical to intrinsic predictability in the mid-latitudes. In the current study, the estimations of practical and intrinsic predictability limits were performed for the tropics. For the reference and comparison, the numerical simulations with the standard deterministic convection scheme were included, also conducted by Selz et al. (2022).

The study is organized in two parts. The objective of the first part is to explore the representation of the tropical waves in the simulations with the stochastic convection scheme using the Hovmöller diagrams and Wheeler-Kiladis space-time spectral analysis. The second part of the study is devoted to predictability time limit estimation for the tropics and achieves the following objectives:

- perform estimates of the practical and intrinsic predictability limits in physical space and investigate the transition from the current practical to the intrinsic predictability;

- perform estimates of the intrinsic predictability limits in spectral space and provide assessments of the slope of the background kinetic energy spectrum;

- investigate the role of spectral slope in error propagation and predictability limits by means of the simple Lilly model.

The structure of the study is as follows: chapter 2 briefly describes the employed data sources and experimental design. The tropical waves representation in the numerical simulations is presented in chapter 3, including the

theoretical background, methods of wave identification and obtained results. Chapter 4 is dedicated to the predictability limit estimations. In chapter 5, the obtained results both for the wave representation and predictability estimations are summarized and discussed.

Chapter 2

Experimental setup

In the current study, three sources of data have been employed: numerical simulations performed using the ICOsahedral Non-hydrostatic Model (ICON) with the Plant-Craig (PC) stochastic convection scheme, numerical simulations performed using ICON with the Tiedtke-Bechthold (TB) deterministic convection scheme, and ECMWF Reanalysis v5 (ERA5) set of data. The applied numerical simulations have been conducted by Selz et al. (2022) to the investigation of the practical and intrinsic predictability in the mid-latitudes.

The chapter contains a description of the used data sources and performed experimental setup. The first section of the chapter provides a review of ICON and the stochastic convection scheme. Section 2.2 is devoted to a brief overview of the deterministic convection scheme and ERA5 data system. The experimental design and the details of performed simulations are described in the last section.

2.1 Numerical model and stochastic convection scheme

ICON is a global numerical weather prediction model jointly developed by the German Weather Service (DWD) and the Max Planck Institute for Meteorology (MPI-M), described by Zängl et al. (2015). The non-hydrostatic dynamical core in ICON is built on an icosahedral-triangular Arakawa C-grid that provides a nearly homogeneous coverage of the globe. Time integration in the model is performed explicitly, with the exception of terms describing vertically propagating sound waves. In addition, high computational efficiency is achieved by time-splitting between the dynamical core and tracer advection, physics parametrizations, and horizontal diffusion. Therefore, the so-called slow-physics processes are evaluated from parametrization schemes on longer time steps, and between two subsequent parametrization calls, received tendencies remain constant in the dynamical core.

In the current study, ICON with 90 vertical levels and spatial resolution of approximately 40 km (R2B6) has been implemented. The simulations with spatial resolution, approximately 20 km (R2B7), for the Wheeler-Kiladis timespac, have been performed additionally. The ICON model setup did not include an ocean model, therefore the sea surface temperatures were fixed and

provided with the initial conditions. The TERRA land-surface scheme (Heise et al., 2006) supplemented with a multi-layer snow scheme and multi-layer soil scheme with a tile-based approach to take into account the land-cover variability at the subgrid scale has been implemented. The TERRA settings also included lake and sea ice models. The cloud microphysics was presented by the five-category prognostic scheme described by Seifert (2008). Since the implemented ICON model resolutions are not convection-permitting, two convection parametrization schemes were applied: the PC stochastic convection scheme (Plant and Craig, 2008) and the TB deterministic convection scheme (Tiedtke 1989; Bechtold et al. 2008). Furthermore, the ICON setup also includes the following parametrizations (reformulated according the model requirements): the fast-physics parametrizations described by Doms and Schattler (2004), the turbulence scheme (Raschendorfer, 2001), the Lott and Miller (1997) subgrid-scale orography scheme, the Orr et al. (2010) non-orographic gravity-wave drag scheme, and the Rapid Radiation Transfer Model radiation scheme (Mlawer et al., 1997).

Although the simulations for the two convection parametrization schemes have been performed, the main object of the current study was the simulations with the PC convection scheme. The TB deterministic convection scheme is a standard parametrization scheme for convection that has been introduced as a reference for comparison with the stochastic scheme and will be described in the following section. Next, a brief overview of the theoretical bases for the PC convection scheme are presented. A complete description has been made by Craig and Cohen (2006) and Plant and Craig (2008).

There is a need to parametrize convection in global and mesoscale numerical models because the resolved-scale motions in these models cannot reasonably represent the moist convection. Moist convection parameterizations usually apply the local equilibrium hypothesis, according to which the average convection properties in each grid cell can be completely determined as functions of the large-scale resolved model variables. The PC scheme receives as input six variables from the dynamical core: the zonal and meridional wind speeds, temperature, and the concentration of solid, liquid and gaseous water phases. For each grid cell described variables are space-averaged over a suitable region both large enough to contain many clouds and small enough to be representative for the current grid cell. The necessity and advantages of input averaging have been discussed by Keane and Plant (2012) and Keane et al. (2014), but in brief, its purpose is to produce a proper representation of the input large-scale thermodynamic state of the atmosphere: to represent the mean state of atmosphere, and not a state already perturbed during previous iterations. The averaged input determines an equilibrium macrostate and the PC scheme implies that local fluctuations in a cumulus cloud field (microstates) near that state are described by the stochastic variability using the Gibbs canonical ensemble. For convection initiation, the Kain-Fritsch trigger function is used, which, however, is deterministic (Kain and Fritsch 1990; Kain 2004). Within each grid cell, the PC scheme randomly initializes individual up-drafts with a upward mass flux strength determined by a probability distribution function given by:

$$p(m)\mathrm{d}m = \frac{1}{\langle m \rangle}\mathrm{e}^{-m/\langle m \rangle}\mathrm{d}m \tag{2.1}$$

where m is a mass flux per cloud and the angled brackets denote an ensemble average (Craig and Cohen, 2006). The sum of the individual initialized updrafts provides the total upward mass flux M in the grid cell. The average total mass flux $\langle M \rangle$ is obtained with a convective available potential energy (CAPE) closure method, so that 90% of CAPE is eliminated within the closure time scale.

Thus, the stochastic approach should be able to represent both the mean effect of convection and its intrinsic variability, what distinguishes it from deterministic schemes. Selz and Craig (2015b) have demonstrated that accounting for variability provides a better representation of upscale growth of convective uncertainty compared to the TB deterministic scheme, where a significantly reduction of upscale error growth and , consequently, a overconfidence of the model is observed. Higher accuracy of upscale error growth prevents overconfidence of the model and therefore provides more realistic predictability time limits. However, it should also be noted that the scheme does not take into account sub-gridscale convective organization.

2.2 Deterministic convection scheme and reanalysis data

In addition to the numerical simulations with the Plant-Craig stochastic convection scheme, as a reference, the simulations with the Tiedtke-Bechthold deterministic convection scheme were investigated. The TB scheme is a conventional convection parametrization scheme for the most of numerical models, e.g. ECMWF, ECHAM, COSMO, REMO etc. It has been originally developed by Tiedtke (1989) and then has been continuously improved by Gregory et al. (2000), Jakob and Siebesma (2003) and Bechtold et al. (2008), and further also updated depending on the base model. Same as the PC scheme, the TB scheme is the mass flux scheme of a cloud ensemble, so its basic components are also the convection trigger function, the cloud model and the closure assumption. The TB scheme utilizes the bulk cloud model method, so a single cloud model represents an ensemble of clouds. As the scheme is deterministic, it solves a set of ordinary differential equations for convective updraughts and downdraughts (entraining-detraining plume model), considering both the organized and turbulent transfer. The trigger for convection initialization is based on the parcel instability and parcel velocity. The scheme discriminates three different types of convective parametrizations: deep, shallow and mid-level convection, and the closure assumption depends on the type of convection. For instance, for the deep convection the CAPE relaxation closure is applied. Also the TB scheme contains a highly simplified microphysical parameterizations, for instance a conversion of cloud condensate to precipitation is directly proportional to amount of cloud condensate. The mass flux approach in general, and the TB scheme in particular, are the quite powerful and simple methods for convective overturning, which makes it widely used. In contrast to the stochastic scheme, which

also requires the equilibrium distribution and the scale for spatial averaging, the deterministic convection scheme only requires the mean mass flux in a grid cell.

Besides the numerical simulations described above, the ERA5 data also have been considered as a source of climatological reference data. ERA5 is the fifth generation of ECMWF atmospheric reanalysis system, which combines broad amounts of historical observations from 1950 to present time into global scale together with advanced modeling and data assimilation systems, such as model forecasts of the ECMWF Integrated Forecast System (IFS) and 4D-Var data assimilation. The ERA5 dataset contains hourly-averaged values of a large number of atmospheric, land and oceanic climate parameters. The ERA5 data system employs 137 pressure levels from the surface up to 0.01 hPa with the spatial resolution of 31 km. The complete description of the reanalysis data sources is presented in the ERA5 data documentation at www.ecmwf.int. In current study, the ERA5 data sets have been used as reference point for the tropical waves representation and as the climatological reference data for predictability time limit estimations.

2.3 Design of experiments

The global numerical simulations created with the ICON model both for the Plant-Craig stochastic convection scheme and Tiedtke-Bechthold deterministic convection scheme have been carried out. The initial conditions for the simulation have been taken from the ECMWF ensemble of data assimilation (EDA) system (Isaksen et.al, 2010). The EDA creates a 50 member ensemble of initial conditions and the members are presented with assimilated observations perturbed by the random noise given by the probability density function of observation error. Due to high computational and volume costs, only five members of the ensemble have been randomly selected for this study. To investigate both the practical and intrinsic predictability and also the transition between them, following Selz et al. (2022), a series of experiments has been performed with rescaling the perturbations in the initial condition by five different factors: 100%, 50%, 20%, 10% and 0.1%. The coefficients indicate the percentage taken from the initial state of the EDA. Thus, the experiments with the 100% rescale factor correspond to the current practical predictability, and the 0.1% rescale experiments are the closest estimate for the intrinsic predictability time limit in the current study. The list of all experiments with the corresponding labels is presented in the Tab. 2.1.

For the sufficient representation of results, 12 simulation cases, each contains five ensemble members, have been investigated in the current study. The cases were distributed over one year, namely from October 2016 to September 2017, and each case consisted of 31 subsequent days starting from the first day of each month, e.g. 1th of October, 1th of November, etc. (same as in Selz 2019; Selz et al. 2022). Because of available computational and volume options and the required large number of simulations, it was not possible to apply the spatial model resolution permitting for convection (resolution $\approx$ 40 km has been applied), which was the reason for using the convection parametrization

Experiment label	Rescale factor	Convection scheme	Singular vectors	ICON lead time	ICON resolution	Number of members	Number of cases
100%PC	100%	PC	–	31 days	R2B6	5	12
50%PC	50%	PC	–	31 days	R2B6	5	12
20%PC	20%	PC	–	31 days	R2B6	5	12
10%PC	10%	PC	–	31 days	R2B6	5	12
0.1%PC	0.1%	PC	–	31 days	R2B6	5	12
100%TB	100%	TB	–	31 days	R2B6	5	12
10%TB	10%	TB	–	31 days	R2B6	5	12
0.1%TB	0.1%	TB	–	31 days	R2B6	5	12
100%svPC	100%	PC	+	31 days	R2B6	5	12
0.1%longPC	0.1%	PC	–	90 days	R2B7	1	1
0.1%longTB	0.1%	TB	–	90 days	R2B7	1	1

Table 2.1: List of performed ICON experiments with the corresponding labels.

to more properly represent unresolved convection-scale motions. Since, the current study investigated intrinsic predictability, the possible effects of the model errors were not taken into account and the perfect model assumption was implied. As mentioned above, the stochastic convection scheme better represents the upscale error growth from convection compared to the deterministic convection scheme (Selz and Craig, 2015b), therefore stochastic convection scheme may reduce the model error from the improper production of corresponding part of error growth at high resolutions. It should be noted that in the current study, employing the stochastic convection scheme is an attempt to make the assumption of the ideal model more accurate, and not an attempt to identify any model error.

The ensemble (ENS) system at ECMWF is characterized by an addition of the singular vectors to the initial conditions set, which are a set of perturbations that grow most rapidly over a finite-time interval and determine the local instability properties. Singular vectors affect only dry part of the linearized model and can be evaluated through the singular value decomposition of the so-called forward tangent linear operator (Diaconescu and Laprise, 2012). In the ENS system, the representation of singular vectors is different for the tropics and extratropics. The perturbations combine the 5 and 50 leading singular vectors over the tropics and extratropics, respectively, and the special version of the singular vectors are employed to specify uncertainties in the moist processes typical for the tropics, e.g. tropical cyclones (see the documentation at www.ecmwf.int for more details). However, since singular vectors can partially compensate for the shortcomings of the model error representation, and the model in this study is assumed to be perfect, adding them to the initial conditions is under discussion. Furthermore, with the rescaling of the initial condition uncertainty, the relevance of the singular vector rescaling is disputable. Therefore, singular vectors were not included in the experiments, except for an additional 100%svPC-experiment to investigate their effect on predictability time limit estimations (Selz et al. 2022).

Thus, as the main object of current study was the stochastic convection scheme, the numerical simulations with the stochastic scheme have been conducted for all five different rescaling coefficients and, as mentioned above, one more additional experiment has been carried out for a 100% rescale factor, tak-

ing into account the singular vectors. Besides the different perturbations in the initial condition, a different random seed of the convection scheme has been applied for every ensemble member for different representation of convective clouds within one macrostate. The numerical simulations with the deterministic convection scheme served as the control and reference simulations, so only 100%, 10% and 0.1% rescale factors have been considered. Insofar as the applied convection scheme is deterministic, no addition of further diversity is required. The tropical wave representation studies used 0.1%-experiments for both schemes and took ERA5 data for the same cases. In the assessment of the predictability time limit estimations all rescale experiments have been taken into account.

As additional control experiments for a tropical wave representation, the long-run numerical simulations both for the PC and TB convection schemes for a longer period have been conducted: 90 days with initialization date of 1th of July. Since this investigation exclusively applied the simulations with a 0.1% rescale factor, the long-run simulations were only performed for the 0.1% scale of the initial condition uncertainty and the ICON model has been operated with resolution $\approx$ 20 km (R2R7).

Chapter 3

Tropical waves representation

This chapter is dedicated to the representation of the tropical waves in the simulations with the stochastic convection scheme. Section 3.1 describes the basic theoretical concepts of tropical meteorology concerning tropical waves as an important aspect of tropical weather and climate. In section 3.2, the identification of different types of tropical waves in the simulations with the stochastic convection scheme has been performed.

3.1 Theoretical background

This section begins with general aspects of the mean atmospheric circulation in the tropics. In subsection 3.1.2, the Matsuno theory of free equatorial waves is explained, which is the basis for understanding the dynamics of equatorial waves. The last subsection is devoted to convectively coupled equatorial waves with its characteristics and their connection with the Matsuno theory.

3.1.1 Atmospheric circulation in the tropics

The Earth's atmosphere is climatologically inhomogeneous, which is primary associated with the orientation of the Earth's rotation axis relative to the Sun and determines the amount of incoming solar radiation reaching the Earth's surface. On the equator, the sunlight reaches the surface almost perpendicularly, then with increasing latitude, the angle of incidence decreases, thus the sunlight warms the area near the equator much more than the poles. Taking into account the amount of Earth's outgoing radiation, which is also latitude dependent, there is an excess of net radiative energy near the equator and its deficit at higher latitudes. Because the surface-atmosphere system is in thermal equilibrium, there is a mean energy transport to the pole by the atmospheric circulation. The magnitude of the Coriolis force also varies in different parts of the Earth: the Coriolis force is much weaker at the equator than at higher latitudes. Thereby, although the atmosphere is a continuous system, based on the general characteristics of the mean atmospheric circulation and forcing in different regions, the particular broad latitude zones may be distinguished. One of these zones is the tropics. The geographic location and extent of the tropical region can be defined in different ways based on different criteria, e. g. direct overhead solar radiation, net positive energy balance, mean monthly

temperatures, etc. (Feeley and Stroud 2018). However, Riehl (1979) proposed the meteorological definition of the tropics as the parts of the Earth where atmospheric processes differ significantly from those at higher latitudes. Based on this definition, tropics can be roughly distinguished from extratropics by the dividing line between the easterly and westerly wind regimes, and the position of the dividing line can vary with longitude and season. Detailed descriptions of the tropical climatology can be found in Holton and Hakim (2013, chapter 11), Smith (2015, chapter 1) and Vallis (2010, chapter 11).

Incoming solar radiation is mainly absorbed by oceans and land areas, however, part of received energy is transmitted to the atmosphere in the form of latent and sensible heat emitted from the surface and transported to the poles by the atmospheric circulation. Thus, despite the excess of radiative energy in the tropics, the tropical atmosphere is characterize as a region of net radiative cooling. The tropical mean meridional circulation consists of the thermally direct Hadley circulation: heated air close to the equator rises up to the tropopause (10-15 km above the surface), where moves to the poles, cools and sinks near the subtropics, around 30°N and S of the equator, then moves to the equator. The trade winds from the Northern and Southern hemispheres come together close to the equator in a so-called the Intertropical Convergence Zone (ITCZ). The ITCZ is a zonal band of deep convection and high precipitation rates, which is characterized by low surface pressure and a large vertical extend of the troposphere.

Additionally, under the action of the Coriolis force, the trade winds in both hemispheres are deviated westward and cause the zonal variations in sea surface temperature (SST), mainly due to wind-driven ocean currents, which leads to a formation of east-west atmospheric circulation cells in the longitude-altitude plane along the equatorial belt. For instance, in the particular significant Walker cell, which located in the equatorial Pacific, air rises over the warm waters of the western Pacific, moves from west to east in the upper troposphere and descends over the cold water of the eastern Pacific. There are also zonal circulation cells, which are driven by zonal pressure gradients due to different diabatic heating over ocean and land areas. Nowadays, the Walker circulation is commonly referred to as a set of zonal circulation cells along the equatorial belt. In some regions, the Walker circulation may dominate over the Hadley circulation and both the Hadley circulation and Walker circulation are subject to small seasonal variations.

Thereby, comparing to the extratropics, the tropics is an area characterized by an excess of solar radiation with smaller seasonal variations, which, together with the large ocean coverage, contributes to an enhanced latent heating of the tropical atmosphere and strong convective activity. A weak Coriolis force provides lower pressure and temperature gradients, so the tropical flow is driven mainly by moist convection. Thus, the mean tropical circulation is presented by the Hadley and Walker circulations.

In addition to the mean circulation, in the tropical atmosphere there are several types of instabilities that are not typical for the extratropical atmosphere, where the nature of the flow is characterized by the predominance of baroclinic instabilities. Tropical instabilities are characterized by a weak geostrophic balance, strong coupling to convection and multiscale interactions.

The most significant tropical instabilities are tropical cyclones, equatorial waves (tropical waves), Madden-Julian Oscillation (MJO) and The El Niño-Southern Oscillation (ENSO).

The present study is devoted to equatorial waves. The equatorial waves are large-scale geophysical fluid waves trapped near the equator, which propagate in zonal and vertical directions and may occur at any height level. They cause oscillations in the pressure, temperature and winds strong enough to impact the large-scale weather and can transmit the influence of local energetic disturbances to wider regions, sometimes spanning the entire equator (Wheeler 2003). The predictability studies also show that predictability time limits of convectively coupled equatorial waves are relatively long and may be a reason of longer intrinsic predictability in the tropics (Judt 2020). The observations show that dispersive properties of equatorial waves are consistent with the dynamics of the Matsuno's Shallow Water (SW) theory (Wheeler and Kiladis 1999), however some aspects of their dynamics are still insufficiently understood. The following is the theory necessary for a basic understanding of the existence and occurrence of equatorial waves.

3.1.2 Matsuno's theory for free equatorial waves

A theory of free dry equatorial waves was first introduced by Matsuno (1966) within the linear SW theory. The SW equations govern the motion of a single thin layer of incompressible fluid of homogeneous density on a rotating sphere and can be derived from the primitive equations. The primitive equations govern the three-dimensional large-scale thermodynamic fields in the stable stratified fluid and, linearized about a motionless basic state, can be mathematically separated into a vertical structure equation and "shallow water" equations. Thus, the SW equations govern the horizontal and timporal evolution of each normal atmospheric mode and the vertical structure equation determines the mode's vertical structure and its so-called "equivalent depth". The equivalent depth provides a link between two separated parts of equations: in the SW equations, the equivalent depth is the depth of the fluid layer required to determine the proper horizontal and timporal structure of each mode. The following is a brief introduction to Matsuno's theory of free equatorial waves. Detailed description of the theory can be found in Matsuno (1966), Kiladis et al. (2009), and Wheeler and Nguyen (2015).

Matsuno considered the inviscid SW equations, where the restoring forces are gravity and a linearly varying Coriolis parameter, $f \approx \beta y$, where y is a distance from the equator, $\beta \equiv 2\Omega/a$, Ω and a are the angular velocity and radius of Earth, respectively (β-plane approximation). Thus, the linear SW equations for a particular vertical normal mode l are

$$\frac{\partial u_l}{\partial t} - \beta y v_l = -\frac{\partial \phi_l}{\partial x}, \tag{3.1}$$

$$\frac{\partial v_l}{\partial t} + \beta y u_l = -\frac{\partial \phi_l}{\partial y}, \tag{3.2}$$

$$\frac{\partial \phi_l}{\partial t} + g h_e \left(\frac{\partial u_l}{\partial x} + \frac{\partial v_l}{\partial y} \right) = 0, \tag{3.3}$$

where u_l and v_l are the zonal and meridional velocities in x and y directions, t is time, ϕ_l is the geopotential, g is the gravitational acceleration, and h_e is the equivalent depth.

Matsuno derived the complete set of zonally propagating wave solutions trapped to the equator, the equatorial waves, from the linear SW equations. Zonally propagating wave solutions are sought are written as

$$\begin{pmatrix} u_l \\ v_l \\ \phi_l \end{pmatrix} = \begin{pmatrix} \hat{u}(y) \\ \hat{v}(y) \\ \hat{\phi}(y) \end{pmatrix} \exp[i(kx - \omega t)], \tag{3.4}$$

where k is zonal wave number and ω is frequency. Substituting (3.4) into the set of equations (3.1)-(3.3) and rearranging them to exclude both $\hat{u}$ and $\hat{\phi}$, the second-order differential equation in $\hat{v}$ can be yielded:

$$\frac{\mathrm{d}^2\hat{v}}{\mathrm{d}y^2} + \left(\frac{\omega^2}{gh_e} - k^2 - \frac{k}{\omega}\beta - \frac{\beta^2 y^2}{gh_e}\right)\hat{v} = 0. \tag{3.5}$$

Since the solutions trapped to the equator are considered and β-plane approximation is applied, the boundary condition for the equation (3.5) is required under which the solutions will decay for a large $|y|$. Together with the boundary condition, the differential equation (3.5) has the same form as Schrödinger equation for a simple harmonic oscillator. For such form of equation, the boundary condition is fulfilled only if the constant part of the coefficient of $\hat{v}$ in (3.5) meets the relation

$$\frac{\sqrt{gh_e}}{\beta}\left(\frac{\omega^2}{gh_e} - k^2 - \frac{k}{\omega}\beta\right) = 2n + 1; \quad n = 0, 1, 2, ... \tag{3.6}$$

The equation gives the relation between zonal wavenumber k and frequency ω for each positive integer n (the meridional mode number), therefore it defines a horizontal dispersion relation of equatorial waves.

Equation (3.6) is cubic with respect to the frequency ω and provides three classes of solutions for specified n and k. At low frequencies, the term ω^2/gh_e can be neglected and (3.6) gives an approximation of one class of solutions as

$$\omega_{ER} \approx \frac{-\beta k}{k^2 + (2n+1)\beta/\sqrt{gh_e}}. \tag{3.7}$$

The wave class corresponding to (3.7) is called equatorial Rossby (ER) waves. Since ω_{ER} is always of opposite sign to k, these waves are only westward propagating.

At high frequencies, the term $-k\beta/\omega$ in (3.6) can be neglected and (3.6) provides the approximations of solutions for two other classes:

$$\omega_{IG} \approx \pm\left[(2n+1)\beta\sqrt{(}gh_e) + k^2 gh_e\right]^{1/2}. \tag{3.8}$$

The wave classes corresponding to the positive and negative root of (3.8) are called eastward inertio-graviry (EIG) and westward inertio-gravity (WIG) waves, respectively.

For the special case when $n = 0$, its exact solutions can be directly obtained from the equation (3.6):

$$\omega_{n=0} = k\sqrt{gh_e}\left[\frac{1}{2} \pm \frac{1}{2}\left(1 + \frac{4\beta}{k^2\sqrt{gh_e}}\right)^{1/2}\right]. \tag{3.9}$$

The positive root corresponds to EIG waves and the negative root provides another class of solutions, mixed Rossby-gravity (MRG) waves, which propagate westward and share the properties of both Rossby and inertio-gravity waves.

The wave class, which is not covered by the solutions of the equations (3.5) and (3.6), is Kelvin waves for which $\hat{v}_l = 0$. The solutions for this wave class is obtained from (3.1)-(3.3) by substituting $\hat{u}$, $\hat{v}$ and $\hat{\phi}$ from (3.4), setting $\hat{v} = 0$ and combining the equations to exclude $\hat{\phi}$. The dispersion relation for Kelvin waves is given by:

$$\omega_K = \sqrt{gh_e}k. \tag{3.10}$$

Since ω_K is always of the same sign to k, the Kelvin waves are eastward propagating. This wave is often labeled as the $n = -1$ wave, because its dispersion relation can also be obtained by assuming $n = -1$ in (3.6).

All five classes of the obtained solutions are shown in Fig. 3.1, where the nondimensional zonal wave number $k^* \equiv k(\sqrt{gh_e}/\beta)^{1/2}$ and frequency $\omega^* \equiv \omega/(\beta\sqrt{gh_e})^{1/2}$ are taken to allow the curves to be plotted irrespective of the values of h_e, β and g. Because equations (3.1)-(3.3) are linearized, any linear combination of the waves obtained above is also a solution to the equations.

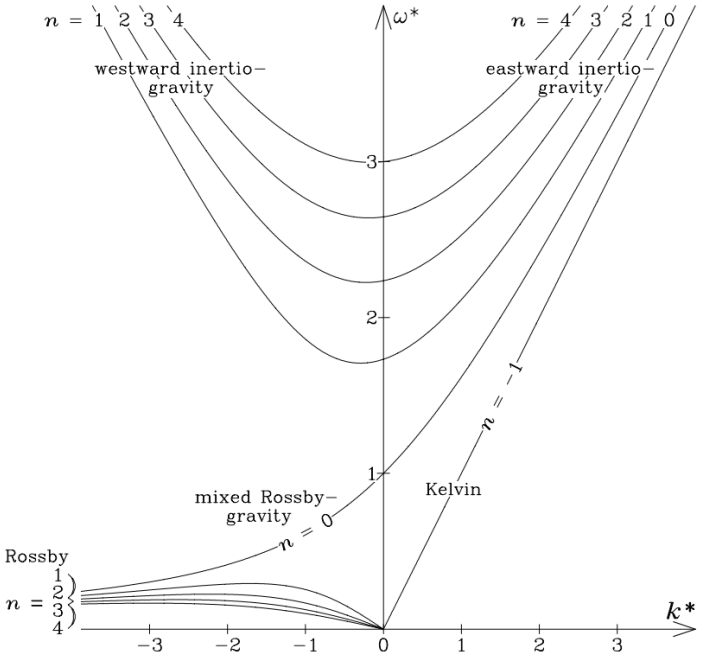

Figure 3.1: Dispersion curves for equatorial waves (up to n = 4) as a function of the nondimensional frequency, ω^*, and nondimensional zonal wave number, k^*. Westward propagating waves (relative to the zero basic state) appear on the left, and eastward propagating waves appear on the right. For consistency with equation (3.6), the Kelvin wave solution is labeled as $n = -1$. Figure is taken from Kiladis et al. (2009), Figure 2.

The full horizontal structures of the equatorial waves, except for Kelvin waves, can be obtained by substituting the solutions for $\hat{v}$ from (3.5) together with the dispersion relations from (3.6) into the equations (3.1)-(3.3) taking into account (3.4). The full horizontal structure of the Kelvin wave may be obtained from equitions (3.4) and (3.1)-(3.3) with $\hat{v} = 0$. Fig. 3.2 shows the full structures for the Kelvin wave, $n = 1$ ER wave, MRG wave, $n = 0$ EIG wave, and $n = 1$ and $n = 2$ WIG waves. All scales and fields have been nondimensionalized by taking the units of time and length as $[T] = (1/\beta\sqrt{gh_e})^{1/2}$ and $[L] = (\sqrt{gh_e}/\beta)^{1/2}$, respectively. The equator runs through the center of each diagram. Essential differences in the general horizontal structures of the equatorial waves can be observed. For the Kelvin and IG waves, the divergence signal is very strong, while the magnitude of their winds and geopotential are relatively weak, so these waves tend to have a more divergent behavior. For Rossby and MRG waves the opposite is true, so these waves have a much more rotational behavior.

Shortly after the Matsuno's theory (Matsuno 1966) was introduced, the first observational evidences for MRG (Yanai and Maruyama 1966; Maruyama 1967) and Kelvin waves (Wallace and Kousky 1968) in the equatorial stratosphere were discovered, which showed a good agreement with the SW theory. Their vertical structures indicated upward energy dispersion, consistent with forcing from below (Holton 1972, 1973), so their initial energy source was assumed because diabatic heating by moist convection in the troposphere. The observed waves were considered to be "free" (or "dry"), since, after occurrence, they were not coupled to convection or any other forcing. However, in the following years, the first attempts were made to detect westward and eastward-propagating disturbances in cloud fields using satellite observations (Chang 1970; Wallace and Chang 1972; Reed and Recker 1971). Later, the more detailed spectral analysis of tropical cloudiness was provided by Gruber (1974), Zangvil (1975), and Zangvil and Yanai (1980, 1981), during which the question was raised about the relationship between deep convection and equatorial SW modes from Matsuno's theory.

However, the detailed observational studies of equatorial waves were not carried out until the 1990s, when the long-period global satellite and operational data analyses became available. First Takayabu (1994) and then Wheeler and Kiladis (1999, hereafter WK99) performed an analysis of the outgoing long-wavelength radiation (OLR) observed from the satellite, a proxy indicator of convection, were able to identify the organized deep convection corresponding to the normal modes of the SW theory. The observed waves were called convectively coupled equatorial waves.

3.1.3 Convectively coupled equatorial waves

Performing the space-time spectral analysis for OLR field, WK99 identified a range of statistically significant spectral peaks corresponding to the dispersion relations from the SW theory with the equivalent depths in the range of 12-50 m, namely the Kelvin peaks, ER peak for $n = 1$, MRG peaks, EIG peaks for $n = 0$, and WIG peaks for $n = 1$ and $n = 2$. Furthermore, they showed that these spectral peaks also have a coherent relationship with the dynamical field

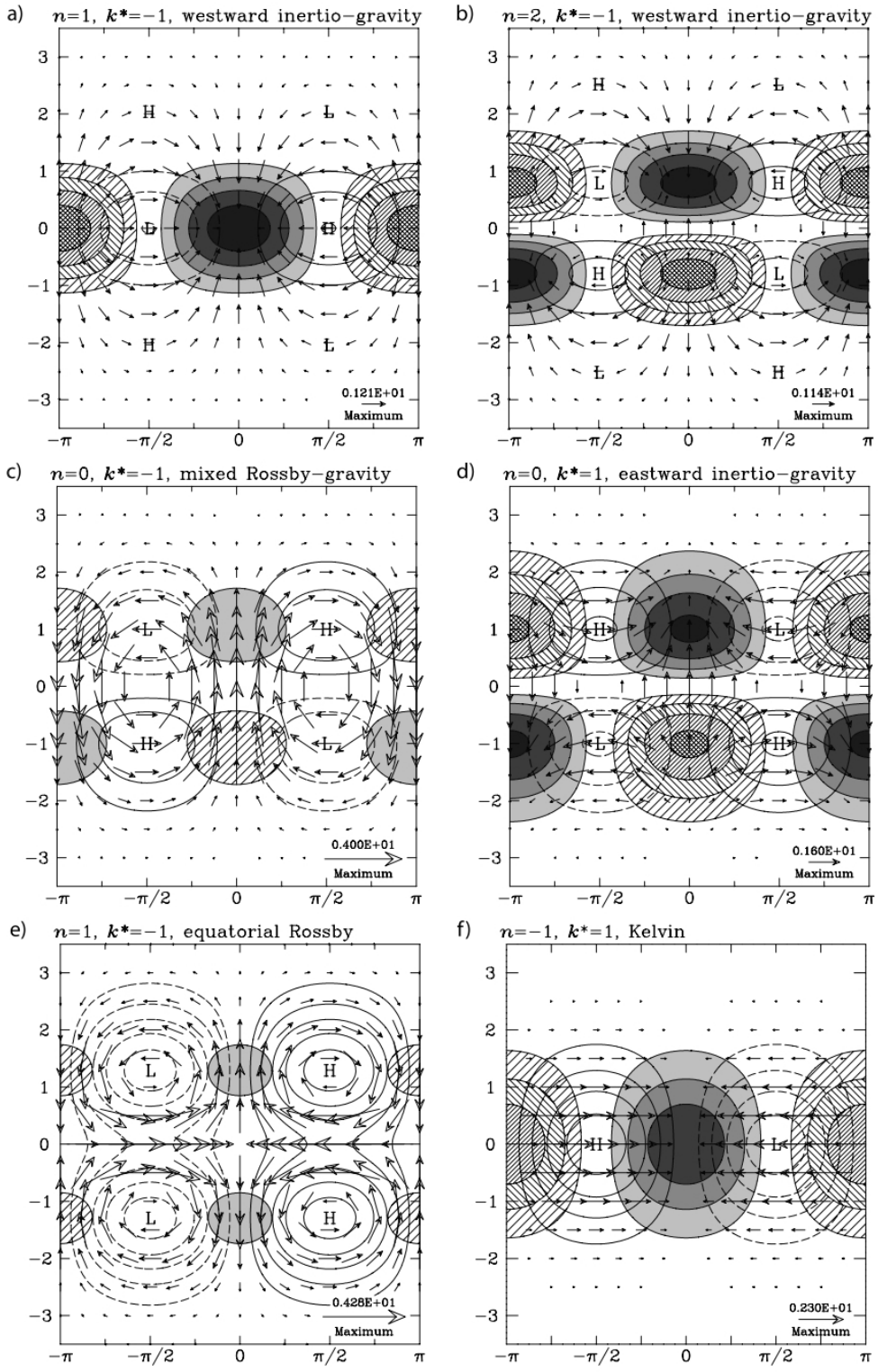

Figure 3.2: Horizontal structures of a subset of the zonally propagating wave solutions to the shallow water equations on an equatorial β-plane (equations (3.1)– (3.3)). Each is shown for a nondimensional zonal wave number, $k^* = \pm 1$. Hatching is for divergence, and shading is for convergence, with a 0.6 unit interval between successive levels. Unshaded contours are geopotential, with a contour interval of 0.5 units. Negative contours are dashed, and the zero contour is omitted. The maximum wind vectors in each panel are specified in the bottom right corner. Figure is taken from Kiladis et al. (2009), Figure 3.

by performing the analysis for the microwave sounding unit temperatures and 1000 hPa geopotential heights. Comparing the obtained CCEWs to uncoupled equatorial waves, which also appear in the dynamical field, they showed that the CCEWs have approximately an order of magnitude smaller equivalent depths. It is assumed that smaller equivalent depths are due to the interaction of convection and dynamics, but the discrepancy between the observed and theoretical equivalent depths has become one of the main problems of the CCEW theory. (Kiladis et al. 2009). Nevertheless, both the dispersion features and the structure of these CCEWs are in sufficient agreement with the linear theory. WK99 identified the common features of each wave type, which have since been confirmed in many studies and further summarized by Kiladis et al. (2009).

Based on WK99 study, the main characteristics of the geographic distribution of CCEWs can be determined. So, the occurrence of CCEWs is widely observed in equatorial regions with wave activity centers over the Indian to western Pacific Ocean sectors, South America and Africa, which undergo a seasonal shift from south of the equator in southern summer to the north of the equator in northern summer. The CCEWs differ significantly in their magnitudes: Kelvin and ER waves are relatively strong, MRG and IG waves are weaker and have similar magnitudes. The Kelvin waves are global in their occurrence and observed throughout the year, but especially in the Atlantic sector and in southern summer. The $n = 1$ ER waves occur mainly in southern summer over the Indian and western Pacific sectors. The MRG and $n = 0$ EIG waves are centered on the dateline, and the $n = 1$ and $n = 2$ WIG waves are centered west to the dateline. The strength of the signal of these waves is similar in the southern and northern summers and $n = 2$ WIG waves are characterized by small seasonal variation. Based on the observed structures, the Kelvin, $n = 1$ ER and $n = 1$ WIG waves are symmetric with respect to the equator and MRG, $n = 0$ EIG and $n = 2$ WIG waves are antisymmetric. This behavior is consistent with the linear SW theory (Kiladis et al. 2009) and can be observed in Fig. 3.2, which shows the horizontal structures of theoretical wave modes corresponding to CCEWs.

On a spatial scale, the CCEWs are distributed from synoptic to planetary scales, with Kelvin waves being the largest and IG waves being the smallest. The Kelvin waves propagates eastward with a typical phase speed of 15-20 m s^{-1} and a time scale of 10 days. The $n = 1$ ER waves are westward-propagating and relatively slow with phase speed of around 5 m s^{-1} and propagation time about 10-15 days. The MRG waves also propagate westward with a phase speed of 15-25 m s^{-1} and propagation time of 3-7 days. The $n = 0$ EIG have a relatively high phase speed of 25-50 m s^{-1} and small propagation time, around 3 days. The typical phase speeds for $n = 1$ and $n = 2$ WIG waves are 15-35 m s^{-1} and time propagation propagation time is up to 2 days.

3.2 Tropical waves representation results

The characteristics of the CCEWs, both from the SW theory and observational studies, may serve for the identification of the individual wave types. Aiming

to explore the representation of the equatorial waves in the simulations with the stochastic convection scheme, the Hovmöller diagrams for total precipitation were applied. The obtained results are discussed in in subsection 3.2.2. The comprehensive identification of CCEWs in the numerical simulations was performed with the space-time spectral analysis and is presented in subsection 3.2.3. The study of the wave representation also included the comparison with the wave representation in simulations with the standard deterministic scheme and reanalysis data. The next subsection provides an overview of the climatology features for these data sources as it is necessary for the interpretation of the results.

3.2.1 Climatology comparison

The convection parameterization not only simulates the deep convection, but also regulates the vertical distribution of heat, moisture, and momentum (Kain and Fritsch 1990), thus precipitation, temperature and wind fields may be significantly affected by the applied convection scheme. To compare the climatology of specified fields in the stochastic and deterministic schemes and reanalysis data, time series for precipitation rate, temperature and wind field at 300 hPa (tropopause region) have been investigated. For each time step in 31-day period averaging was performed over all simulation cases and over all members of the ensemble (for the numerical simulations). To find out whether the effect of convection parameterization on fields differs in different regions, time series were constructed for both the tropics and mid-latitudes. For the tropics, the area between 15°S and 15°N has been selected. For the mid-latitudes, two latitudinal zones have been considered: 40°N-60°N for the northern hemisphere and 40°S-60°S for the southern hemisphere. The final results are averaged over latitudes corresponding to a particular region. For the mid-latitudes the averaging for both hemispheres was performed.

The time series for the precipitation rate are shown in Fig. 3.3. For the tropics, the total precipitation rate according to numerical simulations data is lower than according to reanalysis data, but they both show the same behavior. All three data sources show a clear periodic features: the diurnal cycle. In the tropics, the main contributor to the total precipitation is the convective part. For numerical simulations experiments, the intensity of convective precipitation exceeds the intensity of grid-scale precipitation by several tens of times; according to the reanalysis data, it is only a few times. The convective precipitation rate is significantly lower according to the reanalysis data and the opposite is true for the grid-scale precipitation rate, which is almost negligible for the TB scheme. In the mid-latitudes, the total precipitation rate is several times lower than in the tropics and the diurnal cycle is less pronounced, since tropics are an area of strong convection with a large diurnal variation. In addition, in the mid-latitudes, the contribution of the two precipitation types ddiffers from that in the tropics: most of the total precipitation rate is provided by the grid-scale precipitation. While for the total precipitation rate, both schemes are equally consistent with the reanalysis, a comparison of the convective and grid-scale precipitation rates shows better agreement between the TB scheme and ERA5. In the PC scheme rates of concective and grid-scale precipitation

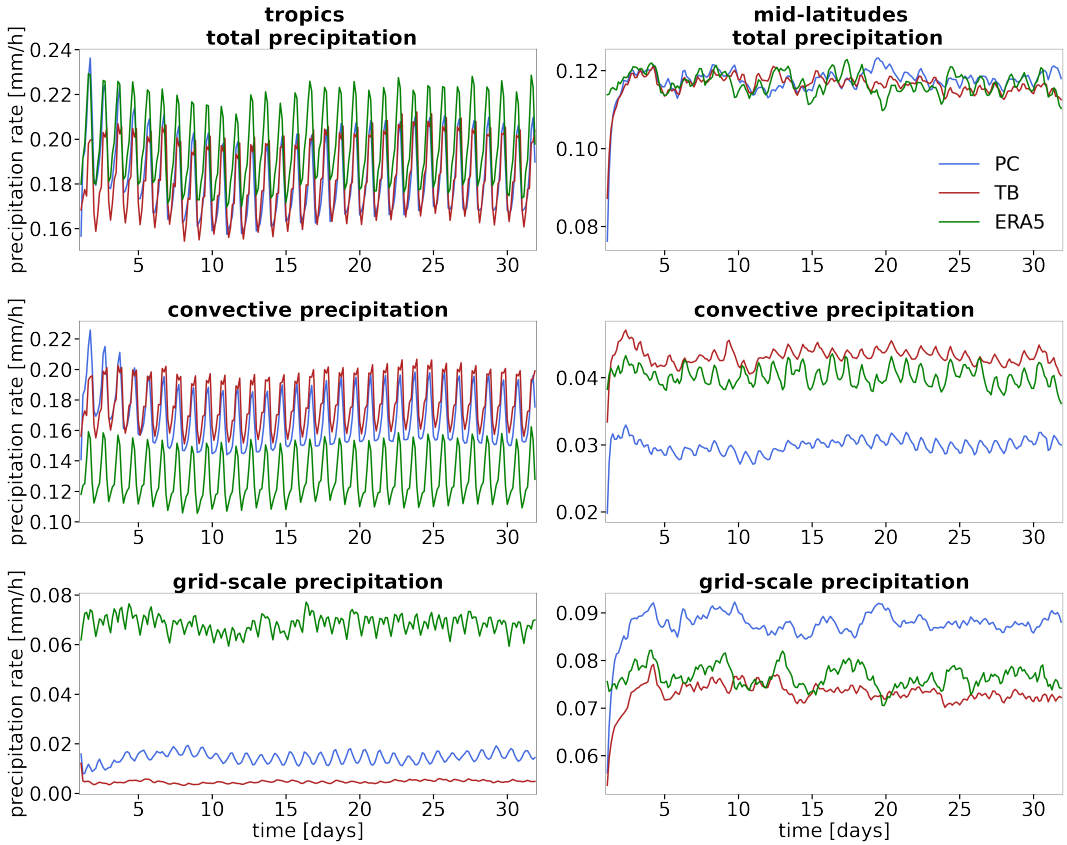

Figure 3.3: Time series of the total, convective and grid-scale precipitation rates for the tropics and mid-latitudes averaged over all 12 and 24 simulation cases, respectively. The blue line is for the stochastic simulations, the red one is for the deterministic simulations. The green line indicates the ERA5 reanalysis data.

are underestimated and overestimated, respectively.

Also, time series were evaluated for a temperature at 300 hPa, which are shown in Fig. 3.4. In the tropics, after initialization of the numerical simulation, there is a significant increase and decrease in the stochastic and deterministic simulations, respectively, until the temperature stabilizes. As expected, there is little variation of precipitation rate over the study period in the tropics. Compare to the reanalysis data, the stochastic scheme overestimates the temperature values, while the deterministic scheme underestimates them. In the mid-latitudes, both schemes overestimate the temperature, but are in a relatively good agreement with each other.

The time series of the zonal and meridional wind components are shown in Fig. 3.5. The most significant differences are observed for the zonal wind component in the tropics. The TB scheme provides relatively close estimates for the first half of the period but after that it begins to underestimate the zonal wind component and a change in the wind regime has been observed over the past few days. The PC scheme shows an overestimation of the zonal wind magnitude over the whole period. Both the stochastic convection scheme and the reanalysis data show the westward moving winds, which is consistent with the wind regime in the tropics. In the mid-latitudes, the zonal wind component

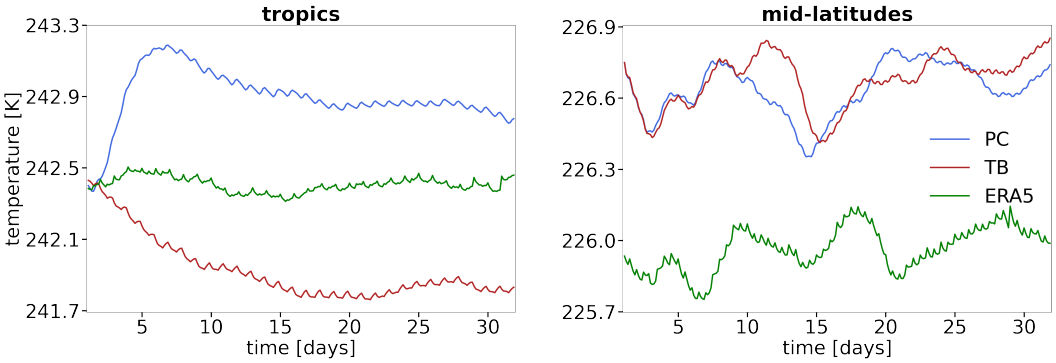

Figure 3.4: As in Fig. 3.3, but for the temperature at 300 hPa.

is much larger than in the tropics due to high pressure and temperature gradients and shows eastward movement. Although both schemes and the reanalysis data are in relatively good agreement for the first 6–7 days, after this period the zonal wind component begins to be underestimated in numerical simulations. The meridional wind components agrees between both schemes and the reanalysis data for the tropics and mid-latitudes.

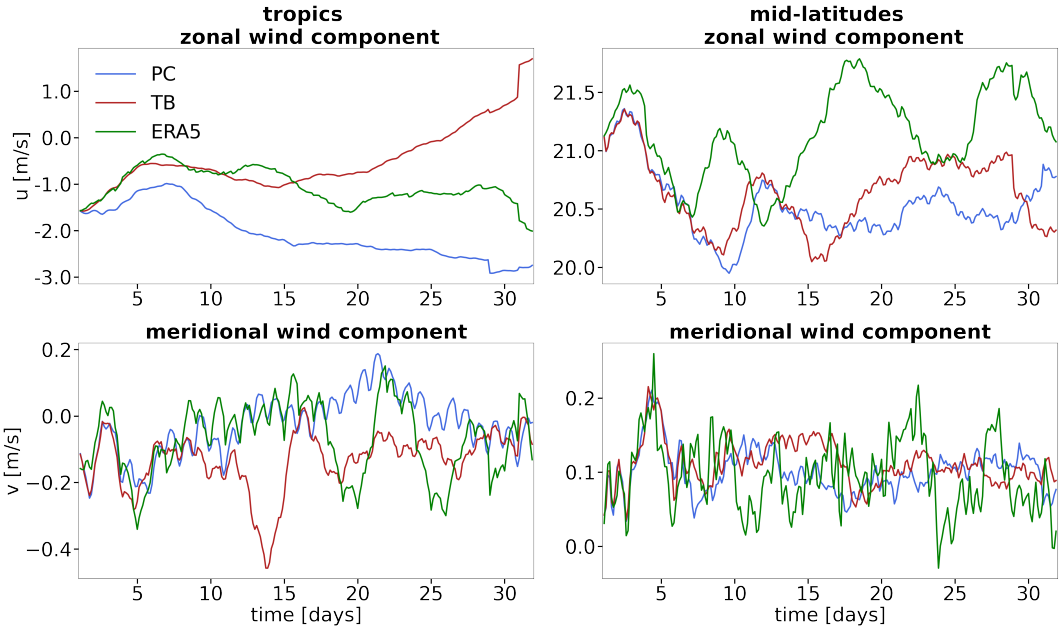

Figure 3.5: As in Fig. 3.3, but for the zonal and meridional wind components at 300 hPa.

Additionally, the spatial structure of the total precipitation values has been investigated. The cumulative values of total precipitation for the entire 31-day period were calculated, averaged over all simulation cases and members (for numerical simulation) and shown in Fig. 3.6. The general features of spacial structures are consistent between the simulations and reanalysisdata, high and low precipitation zones are consistent across the globe. The tropics have wide areas of high rainfall, especially in the Pacific Ocean north to the equator and over the western Pacific sector. In the areas of high precipitation, the reanalysis data usually gives a slightly higher values than the numerical simulations,

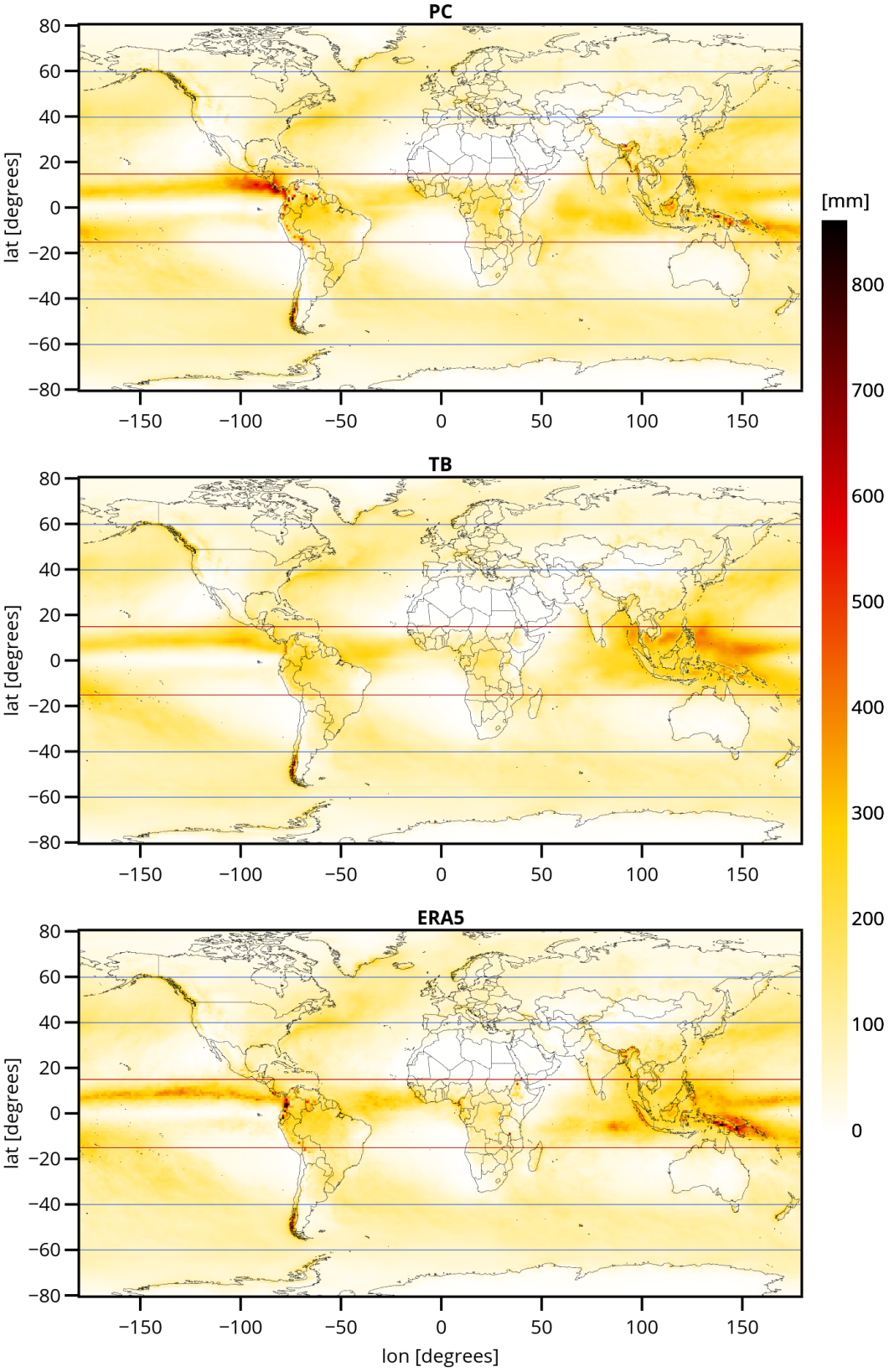

Figure 3.6: Spatial structure of the total precipitation accumulated over the 31 days period. The red lines indicate the boundaries of the investigated tropical region (15°S - 15°N). The blue lines show the mid-latitudes zones in the Northern and Southern hemispheres (40°S - 60°S and 40°N - 60°N).

which is consistent with the underestimation of the total precipitation rate in simulations observed in the time series. The amount of precipitation in the mid-latitudes are significantly lower and more uniform, especially in the Southern hemisphere which is characterized by a large ocean cover. In general, the total precipitation is more intensive over the ocean than over the land. However, between simulations and reanalysis data for some regions, there are differences in the intensity of the total precipitation.

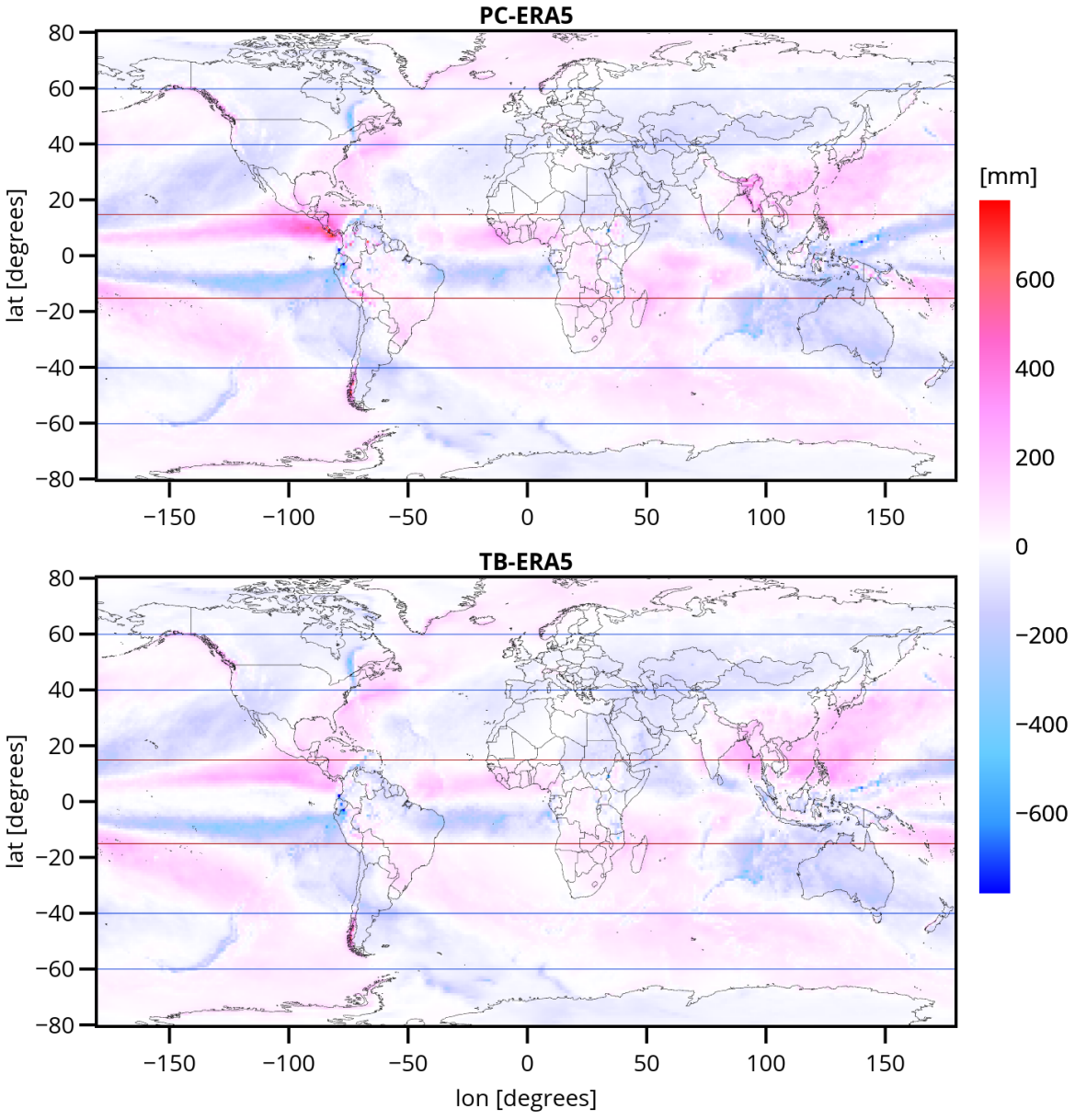

Figure 3.7: Spatial structure of the difference in total precipitation accumulated over the 31 days period between the convection schemes and reanalysis data. Upper figure is the total precipitation difference between the PC scheme and ERA5, bottom figure is the difference between the TB scheme and ERA5.

Fig. 3.7 shows the difference in the amount of the total precipitation between the individual schemes and the reanalysis data. The spatial structures

of the difference provide a relatively good agreement between the simulations. The regions of over- or underestimation of the total precipitation are consistent between the schemes and are most pronounced in the tropics. Thus, over the Pacific and Atlantic Oceans, both schemes overestimate the precipitation north to the equator and underestimate it south to the equator. Over the Indian Ocean the opposite is true. The PC scheme overestimates the area of heavy precipitation over the northern Pacific more significantly than the TB scheme. The main difference between the schemes is observed on the land surface in the regions of Indonesia and Philippines. In the mid-latitudes the variance between the numerical simulations and the reanalysis data is significantly lower. Based on the obtained spatial structures, it can be concluded that, although the spatial structures obtained as a result of the numerical simulations are in good agreement with the reanalysis data, the consistency between convection schemes is higher than between the individual schemes and ERA5.

Summarizing the obtained results of the performed spatial structures of the total precipitation and the time series of the total precipitation rate, wind and temperature, it can be concluded that in the tropics the precipitation fields are more consistent between the simulations compare to the reanalysis data, however it is not possible to make such a conclusion for the temperature and wind fields at 300 hPa. Compared to the reanalysis data, the stochastic scheme underestimates the total precipitation rate but overestimates temperature and the magnitude of the zonal wind component. In the mid-latitudes, there is larger variation between simulations for convective and grid-scale precipitation, but also better consistency for the total precipitation rate, temperature and wind components.

3.2.2 Hovmöller diagrams

According to the performed climatological studies, in the tropics, the representation of the precipitation field in the stochastic and deterministic simulations is in relatively good agreement with the reanalysis data and is even more consistent between schemes. As the first step in the investigation of the tropical waves representation, the Hovmöller diagrams for the total precipitation rate have been performed. The Hovmöller diagrams is a widespread method of plotting meteorological field to highlight the behavior of geophysical waves, in particular tropical waves, displaying both the temporal change and the spatial variability of a meteorological variable. This method has been used in many previous studies of tropical waves behavior (WK99; Kiladis et al. 2009; Kim and Alexander 2013; Roundy 2004; Judt 2020; etc.), commonly applying the Hovmöller diagrams of outgoing longwave radiation or precipitation.

In the current study, the Hovmöller diagrams for total precipitation rate have been performed for each simulation case (31 days period). The diagrams were evaluated for the stochastic convection scheme, for the reference compared with the deterministic convection scheme and reanalysis data. For the investigation, the area between 15°S and 15°N has been selected and only one ensemble member for each case was considered. To represent the field in longitudinal-time domain, averaging was performed over all latitudes. Below are the Hovmöller diagrams for only three simulation cases: January 2017 (Fig. 3.8), April 2017

(Fig. 3.9) and September 2017 (Fig. 3.10). These cases are selected as the most representative and the features, discussed below, are typical for any other cases.

Three longitudinal zones with maximum convective activity are very clearly distinguished on the Hovmöller diagrams: around 30°E, 120°E and 60°W, corresponding to main centers of convection over the central Africa, far western Pacific region and the Amazon basin. The diurnal cycle is also clearly observed and most pronounced at the mentioned longitudinal zones. Another notable feature is the organization of convective activity according to propagation patterns in eastern and western directions. The observed patterns have a wide range of time and space scales and CCEWs can be distinguished among them. It should be noted, that the significant difference in the character of the patterns in the numerical simulations with the stochastic convection scheme is observed: the patterns have more thin and clear character compare to a more diffuse patterns in the numerical simulations with the deterministic convection scheme or reanalysis data.

In the numerical simulations with the stochastic convection scheme, one of the most pronounced wave patterns is westward propagating waves with relatively low phase speed, around 3-6 m s^{-1}, occurring mainly over western Pacific sector and Indian ocean, and with the strong signal during the southern summer (Fig. 3.8). Similar patterns occur also in the eastern Pacific sector with a relative low signal (i.e. Fig. 3.9). According to the described properties, these wave patterns may correspond to a $n = 1$ ER waves. The signs of the ER waves may be also well observed in the ERA5 Hovmöller diagrams, however, in the simulations with the deterministic convection scheme their occurrence is relatively low and the signal is relatively weak (i.e. Fig. 3.9).

Another relatively prominent westward propagating patterns are widely observed in the stochastic simulations, for example in the Fig. 3.10. They are mostly located over the western Africa and have a phase speed, around 15 m s^{-1} and mostly triggered by the diurnal cycle. Similar but weaker structures are also observed over the Amazon basin. According to the phase speed and propagation time, these patterns may correspond to WIG waves and also occur both in the deterministic simulations and in reanalysis data.

As for the MGR and $n = 0$ EIG waves, no significant signs of these types of CCEWs were noted in numerical simulation with a stochastic convection scheme. The eastward propagating wave patterns with phase speed of about 15-20 m s^{-1} over western Africa have been observed in the TB numerical simulations and reanalysis data (Fig. 3.10), which may be consistent with $n = 0$ EIG.

In the reanalysis and the numerical simulations with a deterministic convection scheme, the eastward propagating patterns with phase speed around 20 m s^{-1} and propagation time about 10 days have been observed, mainly over the Pacific and Atlantic Oceans. These patterns may be consistent with Kelvin waves. They are relatively pronounced in the reanalysis Hovmöller diagrams and less pronounced in the diagrams with the deterministic convection scheme (Fig. 3.8 and Fig. 3.9). The signal of these wave patterns is relatively weak, although, these CCEWs are known to be the strongest. In the numerical simulations with the stochastic convection scheme, such patterns are not observed.

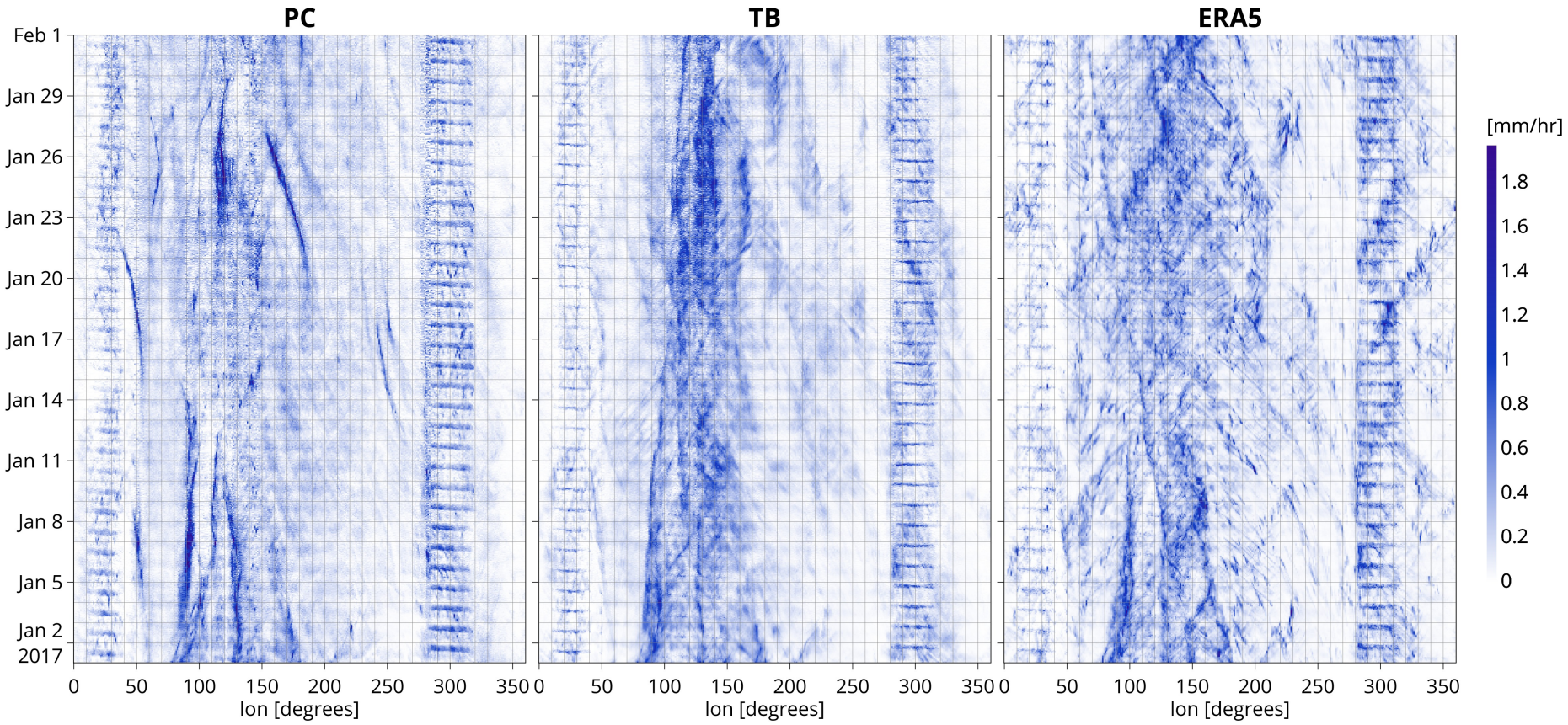

Figure 3.8: Hovmöller diagrams of total precipitation rate averaged between 15°S and 15°N for January 2017. The grid (thin grey lines) have been added to the diagrams with the size of 1 day vertically and 10° horizontally. Longitude is given in degrees East, with 0° East being the prime meridian.

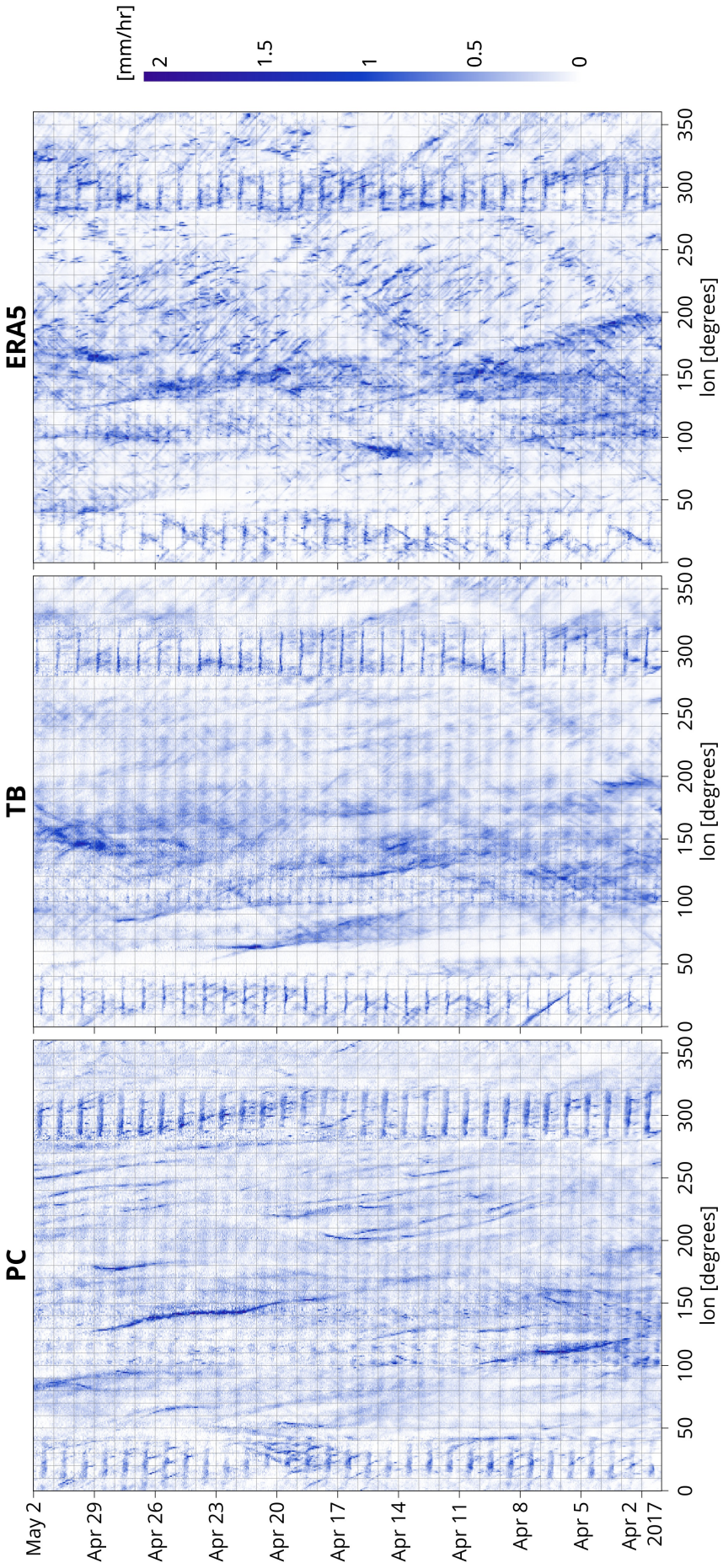

Figure 3.9: As Fig. 3.8, but for April 2017.

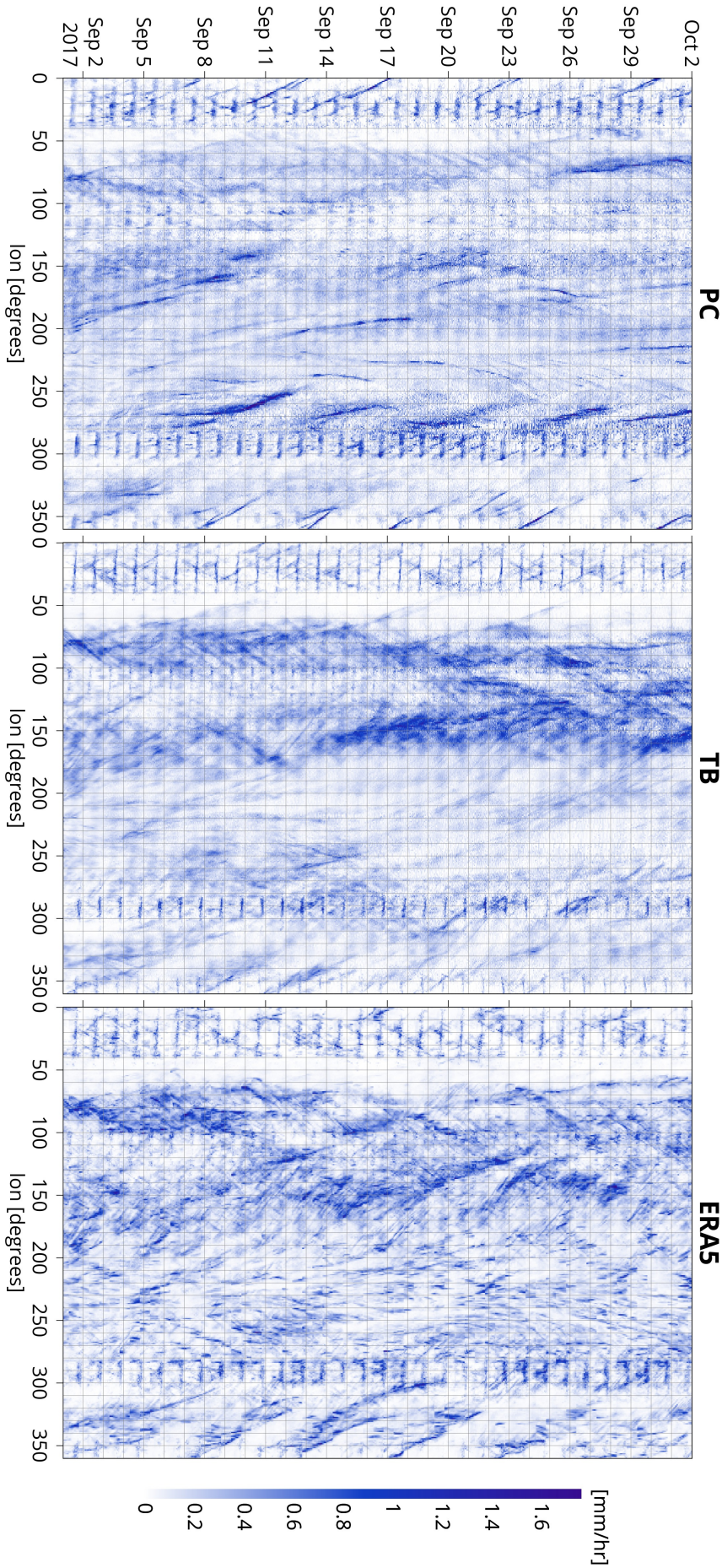

Figure 3.10: As Fig. 3.8, but for September 2017.

Summarizing the above, individual wave patterns can be identified and classified based on their dispersive properties both in numerical simulations and from reanalysis data. The most prominent observed waves are $n = 1$ ER and WIG waves. With regard to the nature and occurrence of individual wave types, the deterministic simulations and reanalysis data are relatively consistent with each other and differ from the stochastic simulations, although the time series and spatial structures showed similarities in representation of the precipitation field which appeared to be higher between the two schemes. It should be noted the absence of Kelvin waves in the numerical simulations with the stochastic convection scheme, however, this type of CCEW is expected to be the most prominent and common. In general, the Hovmöller diagrams for the reanalysis data show a greater variety and clarity of the observed wave patterns than the numerical simulations. However, the Hovmöller diagrams provide only a general view on the tropical wave representation; for a more detailed and accurate study, the space-time spectral analysis should be performed.

3.2.3 Wheeler-Kiladis space-time spectra

The goal of this subsection is to determine the zonally propagating waves in meteorological fields and associate them with the types of equatorially trapped wave modes. Method which is widely used for this purpose is the space-time spectral analysis, which enables detection of a passing wave, including its frequency, length, direction, and amplitude. This method is based on the decomposition of the field dependent on longitude and time into eastward and westward moving components in the wavenumber-frequency domain.

This study implemented the methodology proposed by WK99, where the complex fast Fourier transform (FFT) is applied for the field decomposition. First, the decomposition in zonal planetary wavenumber space is performed by calculating complex FFTs in longitude to obtain Fourier coefficients for each time and latitude. Further, complex FFTs is reapplied, but to the obtained Fourier coefficients and over time, thereby obtaining the wavenumber-frequency spectrum for each latitude. Then the wavenumber-frequency spectrum is summed over the latitude band. Furthermore, according to the SW theory and WK99 is demonstrated, linear equatorial waves are either symmetric or antisymmetric with respect to the equator, so the field can be decomposed to symmetric and antisymmetric components. The gridded fields F, a function of latitude ϕ, can be written as $F(\phi) = F_s(\phi) + F_a(\phi)$, where F_s and F_a are symmetric and antisymmetric components, respectively, and are given by $F_s(\phi) = [F(\phi)+F(-\phi)]/2$ and $F_a(\phi) = [F(\phi)-F(-\phi)]/2$. The method applied in the current study employs decomposition for antisymmetric and symmetric terms, evaluation corresponding spectra and average value estimation.

The study of CCEWs by space-time spectral analysis, allowed to identify tropical waves in the precipitation field (Lin et al. 2006; Hung et al. 2013; Kim and Alexander 2013; Judt 2020; etc.). Using the method described above, the space-time analysis for the total precipitation rate for the numerical simulations with the PC stochastic convection scheme were performed. To compare the presentation of the tropical wave in PC simulations, the same analysis was carried out for the numerical simulations with the TB deterministic convection scheme

and ERA5 data. The investigated simulations cover the 31 days period. To analyze the ERA5 data, the same 31-day simulation cases were used. It should be noted that 31-day segments employed in this study is three times shorter than the segments employed by WK99 (96-day segments), but still sufficient for the timescales of interest. The resulting bandwidth was 1/31 cycles per day (cpd) and 1 unit zonal wavenumber. Also, since available dataset contained only 12 cases, the processed dataset was significantly shorter (1 versus 18 years in WK99). To reduce the noise, the space-time spectra were calculated for each simulation case and then averaged. Spectra for the numerical simulations are also averaged over ensemble members. The latitude band between 15°S and 15°N was determined.

Fig. 3.11 shows the obtained antisymmetric and symmetric zonal wavenumber-frequency power spectra for the total precipitation rate for both simulations with the PC and TB convection schemes and ERA5 data. Power spectra are presented for zonal wavenumbers between -20 and 20 and from a frequency of 1/31 to 0.8 cpd, where the dataset used, according to estimates, contains useful information. The spectra are plotted together with the reference lines of the dispersion curves from the SW theory, which best correspond to the observed features of the wavenumber-frequency. The wavenumber-frequency power spectra are smoother for the numerical simulations compared to the ERA5 data, since they were also averaged by the ensemble members.

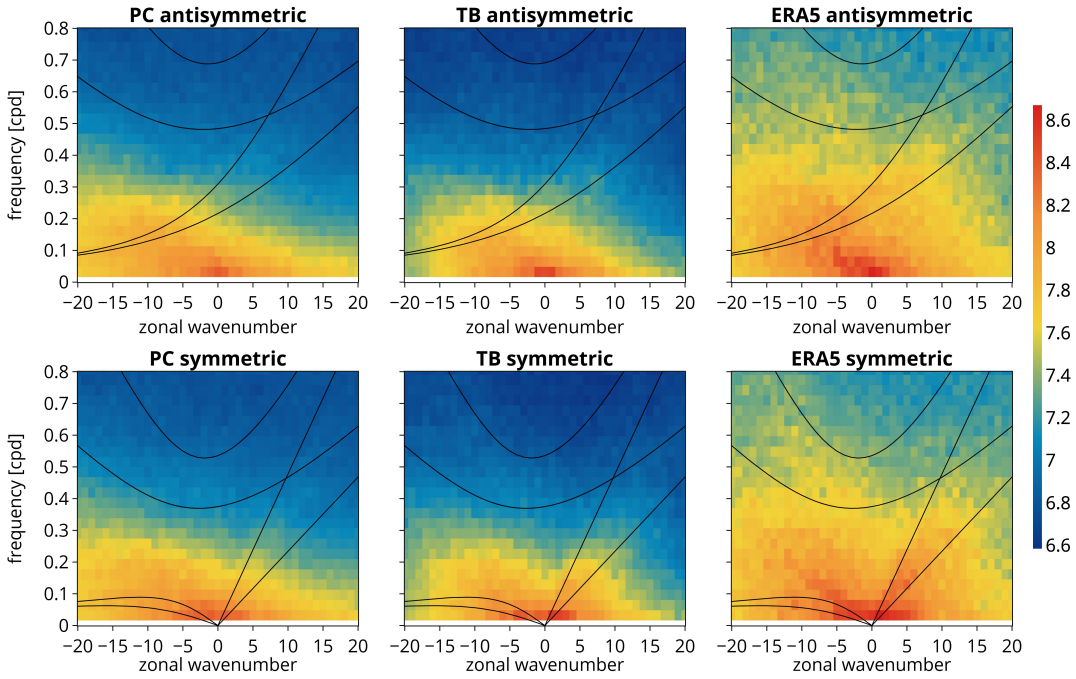

Figure 3.11: Zonal wavenumber-frequency power spectra of total precipitation for simulations with the PC and TB schemes and ERA5 data. On the upper panels are spectra for anti -asymmetric components, spectra for symmetrical components are presented on the lower panels. The base-10 logarithm is taken for plotting. The black lines are dispersion curves from the SW theory with the equivalent depths of 12 and 50 m: in upper panels corresponding to the even meridional mode-numbered equatorial waves and in bottom panels corresponding to the odd meridional mode-numbered equatorial waves.

First of all, the broad red nature of the spectra in both zonal wavenumber and frequency can be seen, which has been shown also in previous studies (e.g. Gruber, 1974; Zangvil, 1975; Takayabu 1994b; WK99). Although, notable differences, which are superimposed upon the background spectrum, between the antisymmetric and symmetric components, as well as eastward and westward propagation directions can be recognized both in simulations and reanalysis data. Thus, in both components and both propagation directions the feature with the greatest power may relate to the Madden-Julian oscillation (Madden and Julian, 1994), which occurs predominantly at eastward wavenumbers up to 5 and in the symmetric components. However, insufficient length of the investigating period of time does not allow to make a certain conclusions. Based on the areas corresponding to the dispersion curves, it is also possible to identify the tropical wave signals. So, the ERA5 symmetric spectrum shows significant spectral peaks of Kelvin waves together with quite weaker $n = 1$ ER and $n = 1$ WIG wave peaks. In the power spectrum of the antisymmentric component of ERA5 total precipitation rate, MRG and $n = 2$ WIG waves are distinguishable, but eastward inertio-gravity waves both for $n = 1$ and $n = 2$ cannot be recognized. The obtained results are in a good agreement with OLR spectra obtained by WK99. In the numerical simulations, the signals of Kelvin, ER and MRG waves are significantly weaker and almost indistinguishable for the PC convection scheme, and no WIG and EIG wave signals are observed. The weak representation of the Kelvin waves in the numerical simulations, especially for the stochastic convection scheme, is consistent with the previous results for the Hovmöller diagrams of total precipitation rate. However, the observed in the Hovmöller diagrams strong signals of $n = 1$ ER and WIG waves does not present in the space-time spectra for the numerical simulations.

Although, the wavenumber-frequency spectra for total precipitation rate show a poor representation of the tropical waves in the numerical simulations and there is a quite significant difference in representation between the stochastic and deterministic convection schemes, the question arises whether the tropical waves disappear in the simulations with the stochastic convection scheme or are they not at all related to? To investigate this question, the wavenumber-frequency spectra for wind divergence were evaluated following the same methodology. Wind divergence were calculated for the three different pressure levels: 300, 200 and 100 hPa. The obtained results of the space-time spectral analysis are presented on the Fig. 3.12, Fig. 3.13 and Fig. 3.14. The main common feature among the spectra for the all pressure levels is the much higher similarity between the two schemes and the reanalysis in comparison with the spectra of the total amount of precipitation. The intensity of the redness of the background spectrum decreases with the increasing altitude of pressure level, however it is more pronounced in the numerical simulations, especially for the PC scheme, at all pressure levels.

Obtained spectra of wind divergence at 300 hPa, for two schemes and ERA5, shows a strong signals of Kelvin, $n = 1$ ER and MRG waves and the strength of the signals is similar among the spectra (Fig. 3.12). On the ERA5 spectrum, a very weak signal of WIG is also observed. A relatively similar situation appears for the 200 hPa pressure level (Fig. 3.13), however a stronger signal of $n = 1$ WIG occurs in the symmetric part of the ERA5 spectrum. The space-time

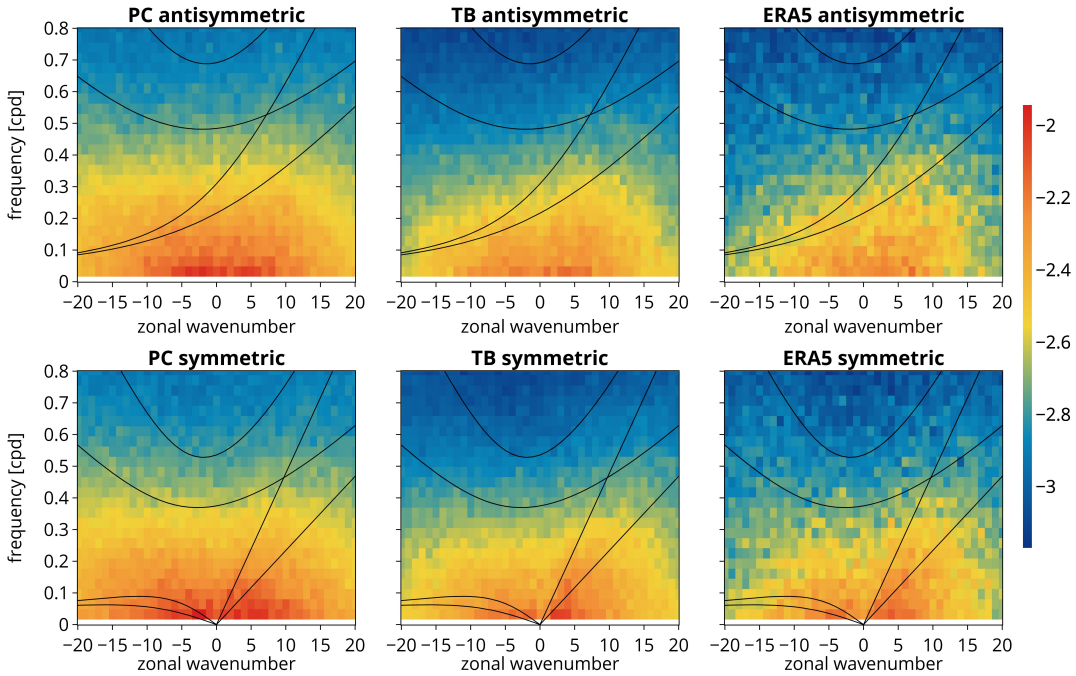

Figure 3.12: As in Fig. 3.11, but for the wind divergence at 300 hPa.

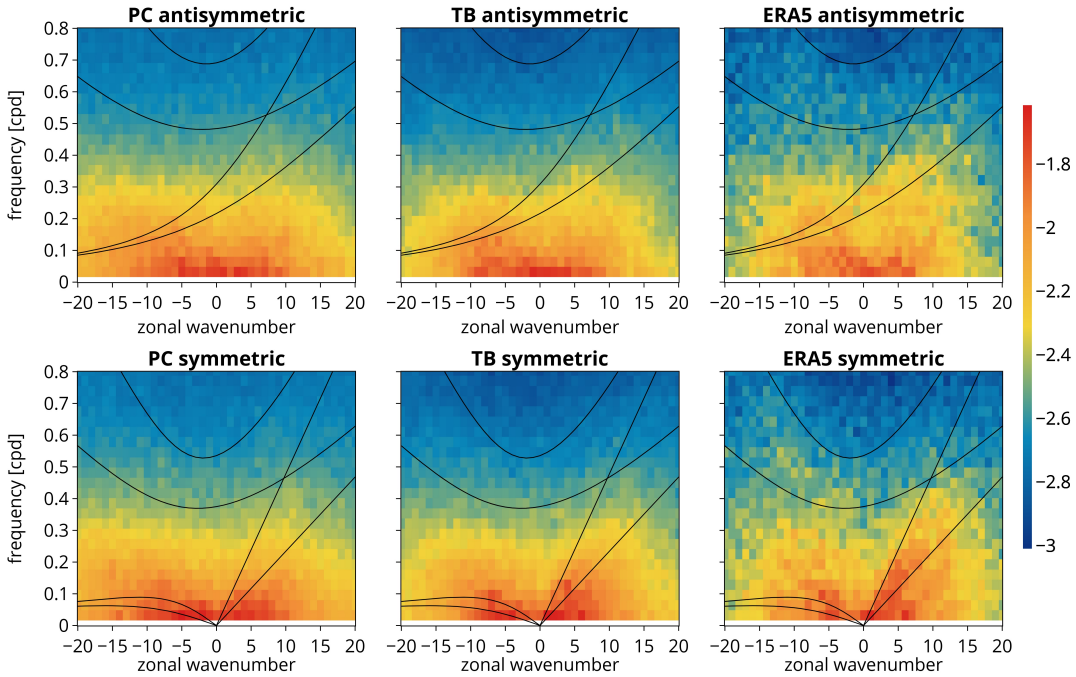

Figure 3.13: As in Fig. 3.11, but for the wind divergence at 200 hPa.

spectra for the 100 hPa pressure level are the most representative. The clear signals of Kelvin, $n = 1$ ER and MRG waves can be observed, but in the numerical simulations the signal is a slightly weaker comparing to reanalysis data. The representation of the WIG waves still remains very poor both in the PC and TB schemes, which may also be caused by the fact that the WIG waves have in general much more weaker signals than other tropical waves.

Summarizing the results, in the space-time spectra for the wind divergence at 300 hPa, 200 hPa and 100 hPa for the numerical simulations with the stochas-

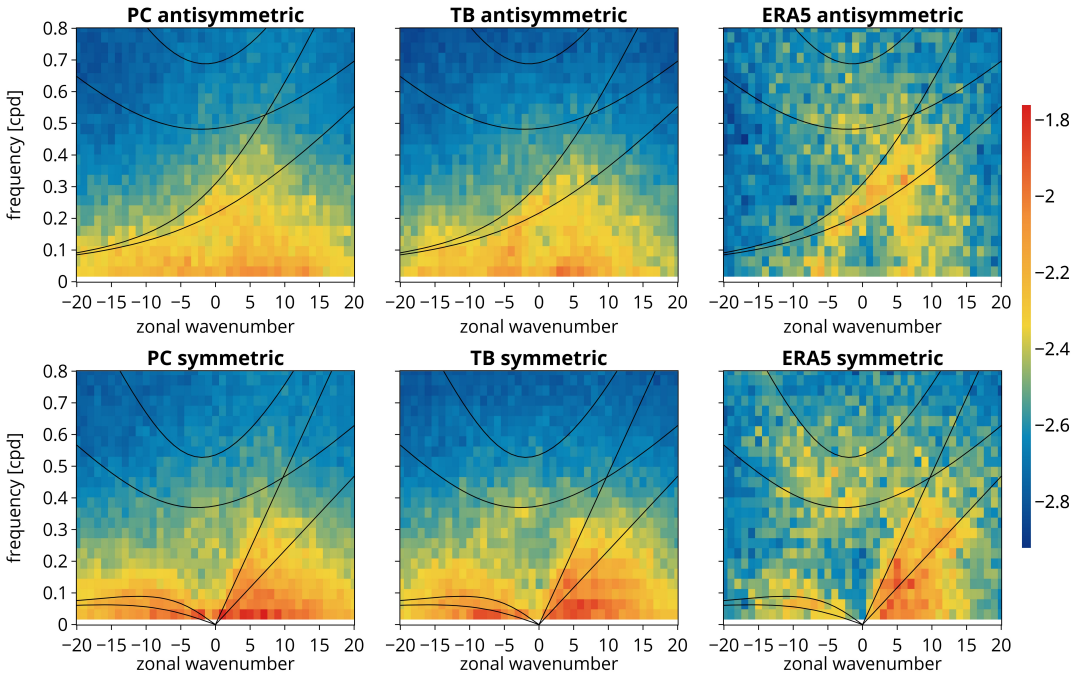

Figure 3.14: As in Fig. 3.11, but for the wind divergence at 100 hPa.

tic scheme, a relatively strong signals of the most prominent tropical waves (Kelvin, $n = 1$ ER and MRG waves) are observed and consistent with the representation of these waves in the numerical simulations with the deterministic convection scheme and reanalysis data. Thus, based on these results, it can be concluded that the tropical waves are presented in the stochastic simulations, but they are poorly connected with convection since they have only a small signal in the spectra of total precipitation.

To further investigate this hypothesis, the additional numerical simulations for a longer time period (96 days) and higher model resolution ($\approx$ 20 km, R2B7, resulting bandwidth 1/96 cpd) were performed for one simulation case and ensemble member. Applying of a longer period of time makes it possible to cover a lower frequency and achieve a higher frequency distribution. Despite the fact that the utilized model resolution is still not convection-permitting, an attempt was made to estimate the influence of a higher resolution on the representation of tropical waves. For these numerical simulations, the time-space analysis of the total precipitation rate and OLR, as a proxy for convection, was performed.

Fig. 3.15 shows the zonal wavenumber-frequency spectra of the total precipitation rate both for the simulations with the stochastic and deterministic schemes. As for the total precipitation rate spectra for a shorter time period and lower resolution, the signals of the Kelvin, $n = 0$ ER and MRG waves are observed and the signals for the PC scheme are slightly weaker compare to TB scheme. The spectra show a small sign of the $n = 1$ WIG waves, which was not noted in Fig. 3.11. Based on the obtained results, a longer investigation time period or higher resolution did not have a significant impact on the tropical waves representation in the field of total precipitation rate. The spectra have a more noisy behavior, since only one simulation case and ensemble member was investigated. The wavenumber-frequency spectra for OLR are shown on Fig.

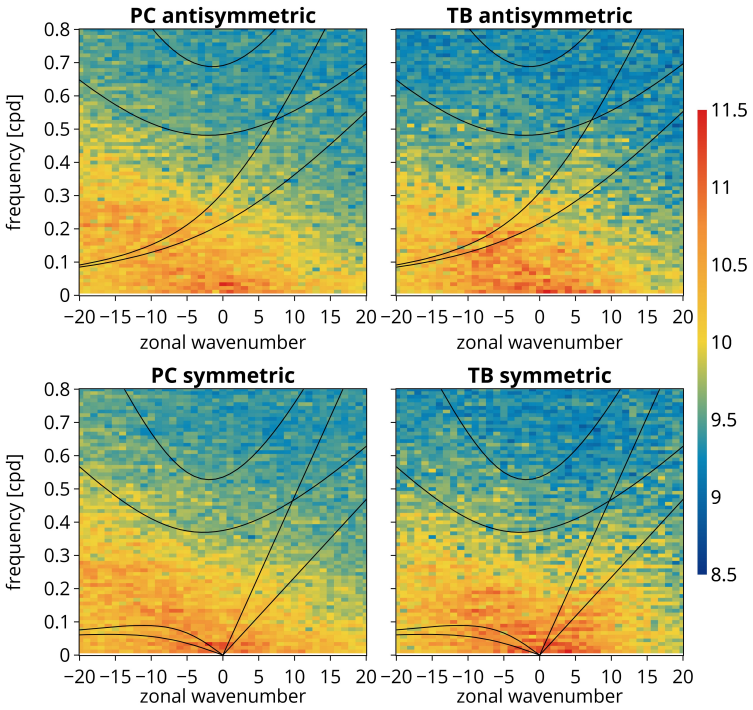

Figure 3.15: As Fig. 3.11, but for the total precipitation rate only for simulations with the PC and TB schemes for long runs with higher resolution.

3.16 and it should be noted that the signals of the tropical waves are very weak both for the PC and TB schemes.

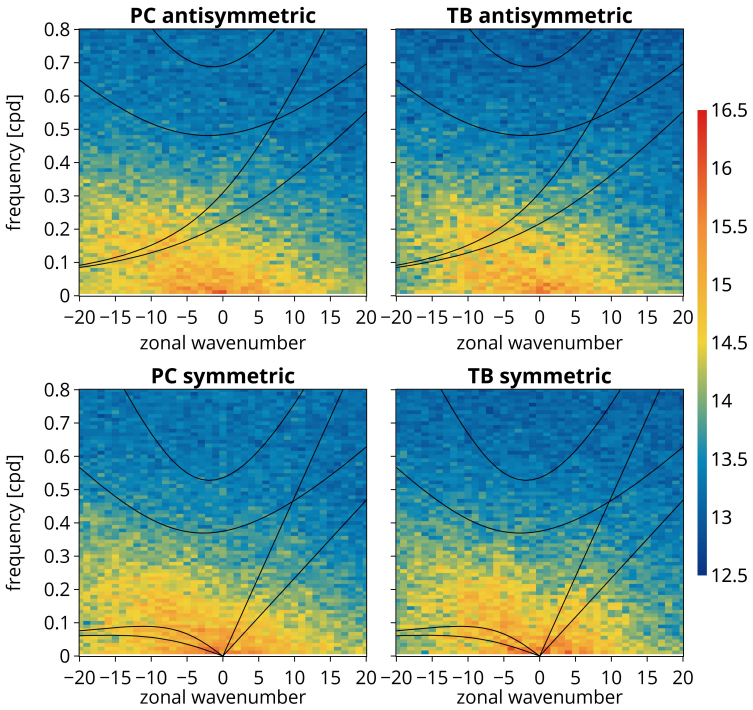

Figure 3.16: As in Fig. 3.15, but for the OLR.

Thereby, in the numerical simulations with the stochastic convection field, the individual tropical waves have been identified from the total precipitation

rate, wind divergence and OLR fields. However, the distinguishable signals of the waves were observed only in the wind divergence spectra. The total precipitation rate and OLR showed only weak signals of the tropical wave. The tropical waves were presented in the numerical simulations but they were not related to convection. Obtained results also show that the representation of tropical waves is slightly better in the simulations with a the deterministic scheme.

Chapter 4

Predictability time limit estimation

In chapter 3, the representation of tropical waves in numerical simulations with the stochastic convection scheme has been explored. The second part of this study is the investigation of predictability time limits in the tropics, which is the subject of this chapter. The first section of the chapter is dedicated to the predictability time estimation both in physical and spectral spaces. In the second section, the role of spectral slope in error propagation and predictability limits is investigated by means of the simple Lilly model.

4.1 Predictability time comparison

In this section the predictability time limit estimation and error growth analysis for the tropics and mid-latitudes are given. The first subsection contains the predictability time estimations for the different initial perturbation experiments. In subsection 4.1.2, the scale-dependent estimations for the intrinsic predictability times have been performed and the error growth rate and spectral energy slope features are discussed.

4.1.1 Predictability time limit estimation in physical space

Comparison of the predictability times for the perturbation experiments with different initial conditions (taking into account only the simulations with 31 days lead time and R2B6 resolution), aiming to study the current practical and intrinsic predictability limits and the transition between them, have been investigated. Estimations of the predictability time limits both in the tropics and mid-latitudes for the predictability limits comparison in these two regions have been evaluated. For the tropics, the area between 10°S and 10°N has been selected. For the mid-latitudes, two latitude zones, 40°N-60°N for the northern hemisphere and 40°S-60°S for the southern hemisphere, have been considered. Tropopause region at the pressure level of 300 hPa has been chosen for the analysis because this level does not affected by complex weather events and relief features but it still have enough energy involved in convective processes.

For predictability time limit estimation, the difference kinetic energy (DKE) approach, as the standard metric for quantifying error growth, has been employed. Since the experimental design envisages not only two simulations but

contains five ensemble members for each simulation case, a generalized definition of DKE that averaging over all possible combination of pairs (Selz 2019) has been applied. Difference kinetic energy per unit mass on a pressure level at specific gridpoint for a case c is given by

$$\Delta e_c(x, y) = var(u) + var(v), \tag{4.1}$$

where the variance across the ensemble members is given by

$$var(u) = \frac{1}{N-1} \sum_{n=1}^{N} (u_i - \overline{u})^2, \tag{4.2}$$

with u and v denoting zonal and meridional wind components, N is the ensemble size and the overbar defines the ensemble mean.

For the tropics and mid-latitudes comparison, domain-averaged DKE error metric has been evaluated as follows:

$$\Delta E_c = \frac{1}{A} \int_A \mathrm{d}A \Delta e_c, \tag{4.3}$$

where A is an area of averaging. Applying $N = 5$ in (4.1) and taking into account (4.2), the domain-averaged difference kinetic energy ΔE_c for every forecast lead time t has been evaluated.

For the ΔE_c saturation limit determination, the comparison with climatological reference data has been performed. As climatological reference data, the ERA5 reanalysis for twenty years has been employed as follows: daily wind data at 0 UTC at the 300 hPa level for the time period from 2000 to 2019 years have been taken (following Selz et al. 2022). For each simulation case, the saturation limit was evaluated over an ensemble of 620 members: for each year, 31 subsequent days were taken, starting on the first day of each month (e.g. 1th of October, 1th of November, etc.). In a similar way, applying $N = 620$, the climatological difference kinetic energy ΔE_c^{clim} has been evaluated. Thus, for the given threshold $\alpha < 1$, the predictability time is determined as the earliest t that satisfies the following condition:

$$\Delta E_c(t) \geq \alpha \Delta E_c^{clim}. \tag{4.4}$$

To reach the saturation limit within the experimental period both in the tropics and mid-latitudes, the threshold value $\alpha = 0.5$ has been chosen.

The predictability time limit estimations both for the simulations with the PC and TB convection schemes have been performed. For each perturbation experiment, 12 predictability time limits for the tropics and 24 predictability time limits for the mid-latitudes (for each of the two latitudinal bands) have been estimated. Finally, mean predictability time limits over all simulation cases and 95% confidence interval of the mean estimates for the tropics and mid-latitudes have been evaluated. It should be taken into account that performed averaging ignores potential seasonal and hemispheric differences. Such differences of the predictability were assumed to be negligible compared to predictability dependence on the flow pattern.

According to the method above, evaluated predictability time limits both for the tropics and mid-latitudes are shown in Fig. 4.1. The predictability time limit curves show similar behavior, but for all perturbation experiments, the predictability time limit estimations in the tropics are about several days longer than those in the mid-latitudes. The obtained predictability time limits for all experiments are presented in the Tab. 4.1.

The 0.1%PC-experiment provides the closest estimations for the intrinsic predictability and gives the predictability time limit values of 16.3 days in the tropics and 12.8 days in the mid-latitudes. Approaching to practical predictability by increasing initial condition rescale factor, the predictability time limit decreases. For the 100%PC-experiment, the predictability time estimated value is 11.0 days in the tropics and 8.6 days in the mid-latitudes. Thus, the differences between intrinsic and practical time limits is approximately 5 and 4 days for the tropics and mid-latitudes, respectively, which may serve as estimations of the potential improvement in predictability time limits by decreasing the error in the initial conditions. It should be noted that according to the obtained results for the tropics, the potential improvement in predictability may be even greater than in the mid-latitudes.

By decreasing error in the initial conditions from 100% to 10% for the simulations in the mid-latitudes, according to Selz et al. (2022), near-linear increasing for the predictability limit times has been observed. Further error decreasing in the initial conditions does not give a significant improvement in predictability, which is typical also for tropics. However, for the rescale factors from 100% to 10%, the reduction in the error causes larger increase in the predictability in the tropics compared to the mid-latitudes. This behavior may lead to better potential predictability improvement, since the additional predictability increase from the error reduction from 10% to 0.1%, on the contrary, is less for the tropics and amounts to 0.4 days (0.7 days for the mid-latitudes).

The experiments for the deterministic convection scheme show similar patterns but with longer predictability time limit estimations, which could be expected due to the noted overconfidence of the TB scheme (Selz and Craig 2015b). For the 10%TB- and 0.1%TB-experiments, the evaluated predictability time limits are about 1.5 days better for the tropics and 1 day better for the mid-latitudes compared to the stochastic simulations. The results of 100%TB-experiment shows differences between two schemes around 0.5 days, but again a slightly larger variance for the tropics. Thus, the presumed overconfidence of the deterministic convection scheme is more pronounced for the tropics. The obtained results also indicate that although the choice of the convection scheme has a negligible effect on the current practical predictability, the effect can become significant with reducing error in the initial conditions (Selz et al. 2022), since the TB numerical simulations showed a possible predictability improvement of about 6 and 5 days for the tropics and mid-latitudes, respectively.

The estimation results of practical predictability described above refer to the numerical simulations without taking into account the singular vectors. However, as noted in section 2.3, the singular vectors are currently operated in ECMWF ensemble forecast system, so the current practical predictability limits may be estimated more accurate by taking into account the singular vectors in the initial condition uncertainty. The simulation study with adding of the

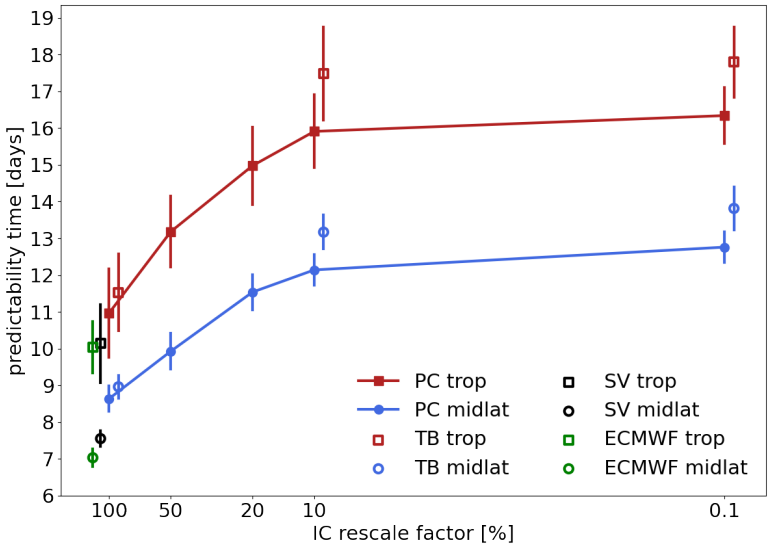

Figure 4.1: Predictability limit time estimations based on climatological reference data evaluated by (4.4) with $\alpha = 0.5$ for the different perturbation experiments. The horizontal axis is logarithmic. The empty markers are slightly shifted horizontally for clarity. The red and blue markers designate predictability time limits for the tropics and mid-latitudes, respectively: full markers for the PC simulations and empty markers for the TB simulations. The black markers designate the singular vector experiment, the green markers - estimations based on ECMWF IFS. The vertical lines show the 95% confidence intervals of the mean estimates.

Convection scheme	Region	IC rescale factors [%]					
		100	100sv	50	20	10	0.1
Plant-Craig	tropics	10.97 ± 1.20	10.14 ± 1.06	13.18 ± 0.97	14.98 ± 1.05	15.91 ± 0.99	16.34 ± 0.76
	mid-latitudes	8.64 ± 0.34	7.55 ± 0.21	9.93 ± 0.49	11.54 ± 0.48	12.14 ± 0.41	12.76 ± 0.41
Tiedtke-Bechthold	tropics	11.53 ± 1.04	–	–	–	17.48 ± 1.27	17.80 ± 0.96
	mid-latitudes	8.96 ± 0.30	–	–	–	13.17 ± 0.46	13.81 ± 0.59

Table 4.1: Predictability time limits in days (Eq. (4.4) for $\alpha = 0.5$) with the 95% confidence intervals of the mean estimates for the different perturbation experiments. The designation "100sv" denotes the predictability time limit estimated for the 100% initial condition uncertainty with inclusion of the singular vectors.

singular vectors (100%svPC-experiment) has been performed, the results of the experiment show that predictability time limit estimations are about 1 day shorter than the estimations for the 100%PC-experiment both for the tropics and mid-latitudes. Thus, the obtained estimations indicate that the potential predictability improvements estimated above may be about 1 day longer for both regions.

In addition to the performed ICON numerical simulations, the practical predictability time limits for the ECMWF IFS for the same simulation cases have been evaluated. The obtained estimations are also shown in the Fig. 4.1

and they are quite close to the the 100%svPC-experiment estimations, which implies the similarity of the current practical predictability limits for the ICON with the stochastic convection scheme and for the ECMWF IFS. Note that these two forecast sets have the same initial conditions, since the 100%svPC-experiment utilizes the initial conditions from the ECMWF's EDA system and the ECMWF IFS includes the singular vectors.

It should be noted that uncertainty for predictability limits are 2-3 times larger for the tropics compared to the mid-latitudes for all simulations that have been performed. This feature can be partly explained by different number of simulation cases: twice as many cases have been evaluated for mid-latitudes (for the northern and southern hemispheres).

4.1.2 Predictability time limit estimation in spectral space

This part of the study is dedicated to the further investigation of the intrinsic predictability limit and uses the simulations with 0.1%-perturbations of the initial condition uncertainty (for the 31 days lead time and R2B6 resolution). An object of the study was both scale-dependent predictability time limits and error growth rates over a spatial scale. The spectral energy slopes for the tropics and mid-latitudes have been estimated and analyzed. As well as in subsection 4.1.1, the area between 10°S and 10°N for tropics and two latitude zones, 40°N - 60°N and 40°S - 60°S, for the mid-latitudes have been considered. Also, the tropopause region at the pressure level of 300 hPa has been chosen for the analysis.

In current study, for investigation of error growth over a spatial scale, spectral DKE has been implemented by applying Fourier transformation for the spatial decomposition of DKE and KE. For each latitude in the tropics and mid-latitudes, the one-dimensional Fourier transform with respect to longitude has been applied. For each region, a constant mean zonal grid spacing was assumed, determined by the zonal grid spacing of the mean latitude: 0°N for the tropics and 50°N/S for the mid-latitudes. Introducing the spatial decomposition, the spectral density of KE at the certain latitude for a case c is given by

$$\tilde{e}_c(k) = \frac{1}{2}(\overline{|\tilde{u}_i|^2} + \overline{|\tilde{v}_i|^2}), \tag{4.5}$$

where $\tilde{u}_i$ and $\tilde{v}_i$ are Fourier coefficients of the zonal and meridional wind components of ensemble member i and are functions of the zonal wavenumber k. The overbars again denote the average of all ensemble members.

Similarly as for the DKE in the physical space, for N-member ensemble, the spectral DKE is generalized by averaging over all possible pairs:

$$\Delta\tilde{e}_c(k) = \frac{N}{N-1}(\overline{|\tilde{u}_i|^2} + \overline{|\tilde{v}_i|^2} - |\overline{\tilde{u}_i}|^2 - |\overline{\tilde{v}_i}|^2), \tag{4.6}$$

namely is equal to a difference between the ensemble mean kinetic energy spectral density and the kinetic energy spectral density of the ensemble mean.

To ensure that the domain-averaged spectral energy densities in wavenumber space are consistent with the domain-averaged energies in physical space,

the spectral KE and DKE have been normalized to satisfy the Parseval identity (Durran et al. 2017). For the KE, the Parseval relation is given by

$$E_c = \frac{1}{A}\int_A \mathrm{d}A e_c(x,y) = \overline{\int_k \mathrm{d}k \tilde{e}_c(k,y)}, \tag{4.7}$$

where $e_c(x,y)$ is the kinetic energy per unit mass on a pressure level at specific gridpoint for a case c. The overbar denotes the latitude average. For the DKE, the Parseval relation is given by:

$$\Delta E_c = \frac{1}{A}\int_A \mathrm{d}A \Delta e_c(x,y) = \overline{\int_k \mathrm{d}k \Delta\tilde{e}_c(k,y)}. \tag{4.8}$$

In contrast to predictability time limit estimation in physical space, a scale-dependent predictability time limit may be evaluated through the KE spectrum without a climatology reference. According to Selz and Craig (2015b), the phases of ensemble members become completely uncorrelated on a certain scale, if their DKE on that scale equals twice the background KE. Thus, the background KE spectrum can be taken as a measure of error saturation and the scale-dependent predictability time limit can be determinated as the earliest t that satisfies the following condition:

$$\frac{1}{2}\overline{\Delta\tilde{e}}_c(t,k) \geq \alpha\overline{\tilde{e}}_c(t,k), \tag{4.9}$$

where $\alpha < 1$ is again a given threshold and the overbar denotes the average over the latitude range. Note that the latitude averaging in (4.7), (4.8) and (4.9) is possible due to the assumption of a constant mean zonal grid spacing.

Thus, for each forecast lead time, the spectral KE and DKE both for the PC and TB convection schemes have been evaluated and normalized. The investigation of the time-averaged KE spectrum, since it is the upper bound to DKE growth rate, has been performed. The evaluated background KE spectra for the tropics and mid-latitudes, averaged over all simulation cases are shown in Fig. 4.2 (upper panel). Comparing two convection schemes it can be noted, that the background KE spectra in the mid-latitudes are almost identical for both schemes. However, in the tropics, on the small scales, the KE is smaller for the TB scheme, but, starting from approximately 4000 km, it get equal to the KE for the PC scheme and then becomes larger. In general, thought, initially on small scales the difference between the kinetic energy in the tropics and mid-latitudes is quite small, it increases towards large scales, and the background KE becomes many times greater in the mid-latitudes. The described behavior can be explained by the different slopes of the energy spectra for the tropics and mid-latitudes.

For the PC scheme, an estimation of the slopes of the energy spectra over a spatial scale with equidistant wavelength intervals on a logarithmic scale has been performed (Fig. 4.2, lower panels). For each interval, the slope was estimated using a polynomial fit function and it should be noted that over a spatial scale, the slope of the energy spectrum was shallower for the tropics. Additionally, the spectral slopes only for scales where neither forcing nor dissipation

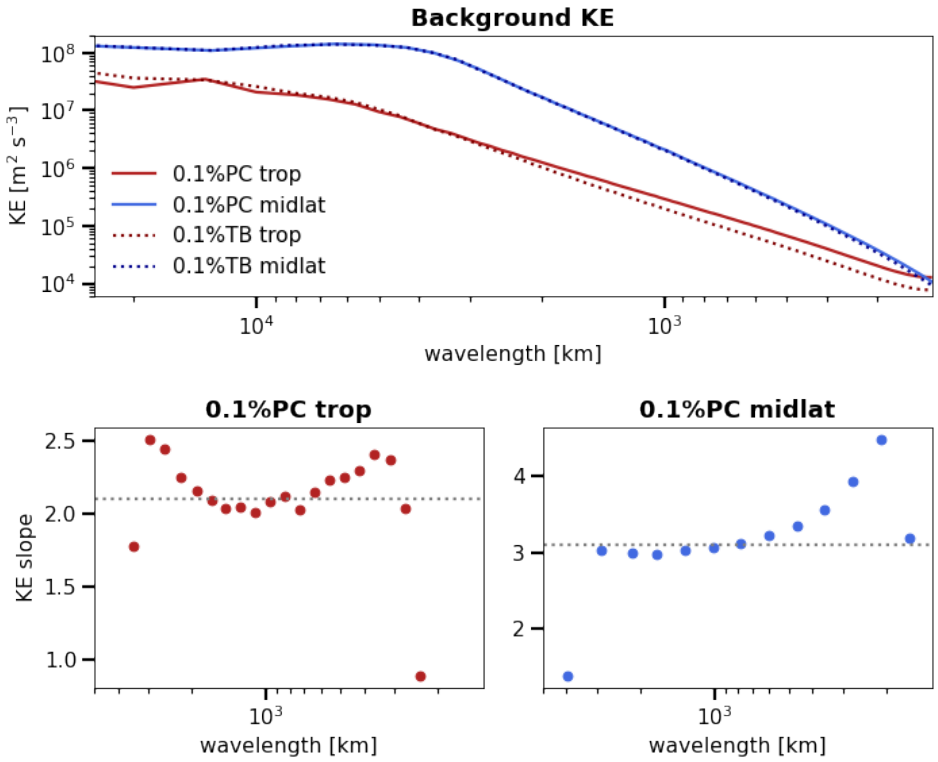

Figure 4.2: Background KE spectra(upper panel) and energy spectrum slopes (lower panels) for the tropics and mid-latitudes. The vertical axis of upper panel and all horizontal axes are logarithmic. The KE slopes are calculated for the equidistant on a logarithmic scale intervals and a representative wavelength of each interval is found as the geometric mean. The grey lines indicate the slopes for the inertial range.

dominates (so-called inertial range) have been estimated. Relying on the results of the Global Atmoscheric Sampling Program described by Nastrom and Gage (1984), the smallest and largest scales of inertial range were defined as 400 and 4000 km, respectively. In current study, for the tropics and mid-latitudes, the scales closest to corresponding wavelengths were selected from the available spectral analysis scales. From the polynomial fitting, KE spectral slope values 2.1 and 3.1 for the tropics and mid-latitudes, respectively have been evaluated. Thus, the energy spectrum slope in the tropics is shallower than in the mid-latitudes, which leads to smaller background kinetic energy at large scales. The similar estimation of the slope in the tropics for the TB scheme provided KE spectral slope value of 2.3, which may explain the larger kinetic energy than for the PC scheme on the large scales, though the kinetic energy on the small scales is smaller. The obtained estimations for KE spectral slope values are partially in agreement with the results in Judt (2020), who also get the shallower spectral slope for the tropics. Using a graphreader tool, the slopes of the background kinetic energy from the Judt's Fig. 5 on the same scales were estimated and the slopes of 1.8 and 2.5 for the tropics and mid-latitudes, respectively, were obtained.

Further, the evolution of the spectral DKE over a time scale for error growth behavior investigation has been analyzed. The corresponding evaluated time

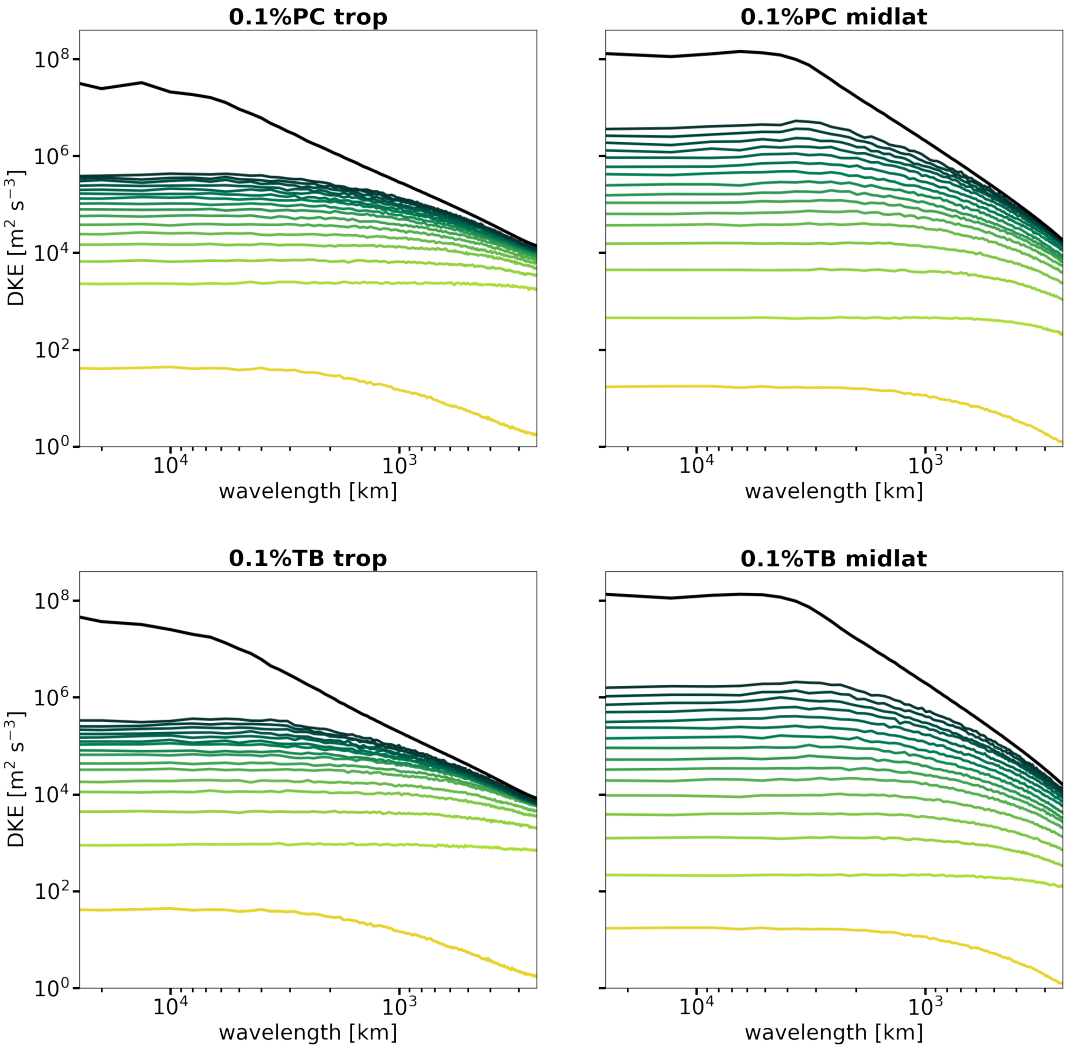

Figure 4.3: DKE spectra for the 0.1%-experiments for the tropics and mid-latitudes, evaluated from (4.6). Both axes are logarithmic. The green lines are the DKE spectra for the first 7 days of the simulation plotted every 12 hours. The yellow lines are the initial condition DKE plotted with magnification of 100 times. All the DKE spectra are divided by 2 to match the background KE spectrum. The black lines indicate the background KE spectra.

evolution of the spectral DKE for the first 7 days of the simulation and background KE spectrum, as it is the upper limit of 0.5DKE, are presented in Fig. 4.3. Both the KE and DKE spectra were averaged over all simulation cases. It can be seen that all DKE spectra shows its increasing with increasing the scale. Towards the large scales from a certain scale, the error energy reaches the maximum and the spectra become plane. It should be noted, that the standard linear definition for the spectral density does not allow to register a pronounced energy maximum. Selz et al. (2022) showed that use of the logarithmic definition ensures its clearer representation. Nevertheless, all experiments that have been carried out in the current study show DKE increasing with time step in the wavelength, at which the growth of the DKE stops. An explanation for the upscale maximum movement can be found by considering the growth rates of

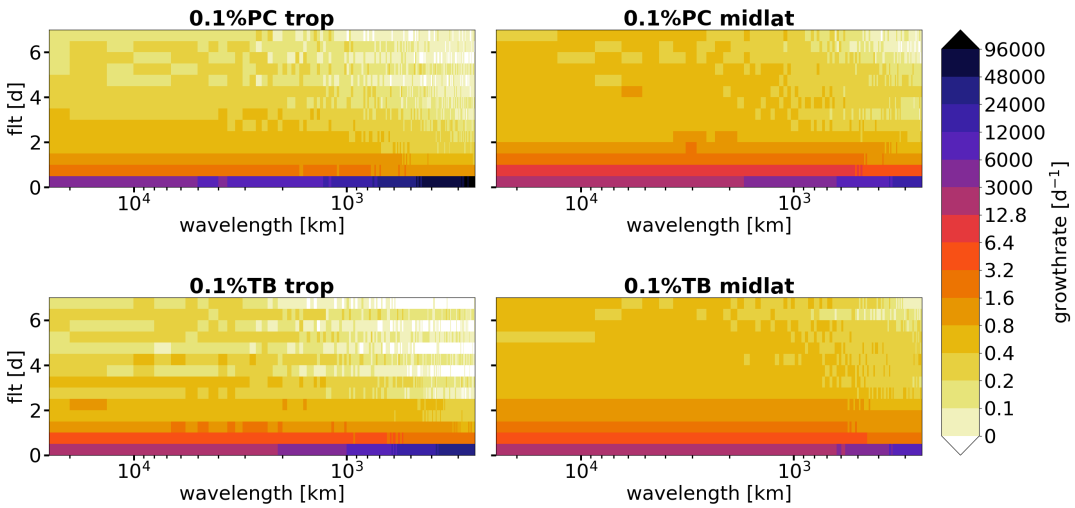

Figure 4.4: Spectral DKE growth rates over forecast lead time(flt) for the tropics and mid-latitudes, plotted for the first 7 days of the simulation. The horizontal axis is logarithmic.

the DKE. Fig. 4.4 shows the growth rates of the spectral DKE for the same period. The deceleration of the error growth with time is observed for all scales, but it is especially pronounced on small scales, where its complete stop can be observed when the saturation limit is reached. Therefore, the error saturation on the small scales causes the error energy maximum to move up the scale.

In first 12 hours of the simulation, the growth rate of the spectral DKE is extremely large both for the tropics and mid-latitudes, especially on the small scales. However, comparing the two regions, in the tropics, the growth rate over all scales and the difference between the growth rate on the small and large scales are many times higher compared to the mid-latitudes, which may be caused by the stronger convection activity in the tropics. After that stage, the significant deceleration of the growth rate is observed and it is more pronounced in the tropics, which can be caused by the lower background KE spectrum. As the growth rate in the tropics is several times lower than in the mid-latitudes, although the initial DKE spectra are larger in the tropics, after one day the DKE equalizes, and then the mid-latitudinal DKE becomes larger. Also, in contrast to the first 12 hours, for both regions, the growth rate on the small scales is less than on the large scales as it approches the saturation limit. In the tropics, the saturation limits are approached faster than in mid-latitudes, and therefore the upscale movement of the error energy maximum is also faster in the tropics.

As it was noted by Selz et al. (2022), the observed upscale error energy maximum movement should not be taken as an indication of the upscale error growth processes, since it is caused by the saturation on the small scales. On the other hand, after a few days of the simulation, an approximately constant error growth over the large scales is observed, especially in the mid-latitudes. The observed in current study constant error growth was also observed in many previous studies (e.g. Durran and Gingrich 2014; Judt 2018; Selz et al. 2022) and was associated with a so-called "up-magnitude" error growth.

Comparing the evolution and growth rate of the spectral DKE for the PC

and TB convection schemes, it was noted that in the mid-latitudes, although the background KE spectra are similar for both convection schemes, the TB scheme provides the lower DKE spectra for both regions, which may again leads to its overconfidence. Similarly, in the tropics, the DKE values in the spectra are lower for the TB scheme, however the background KE values are also smaller on the small scales, which leads to a faster error saturation on small scales (Fig. 4.4). Although, no significant differences in the growth rates between the two schemes are observed in the mid-latitudes, in the tropics, the lower DKE spectra values cause the much lower growth rate in the first 12 hours of the simulation.

Finally, scale-dependent predictability time limits have been estimated based on the spectral analysis of the KE and DKE values, applying equation (4.9) with $\alpha = 0.5$ again to reach the saturation limits within the experimental period both in the tropics and mid-latitudes. Fig. 4.5 shows the predictability time limits over spatial scale for the tropics and mid-latitudes both for the PC and TB schemes. The mean predictability time limits were evaluated over all simulation cases as described above.

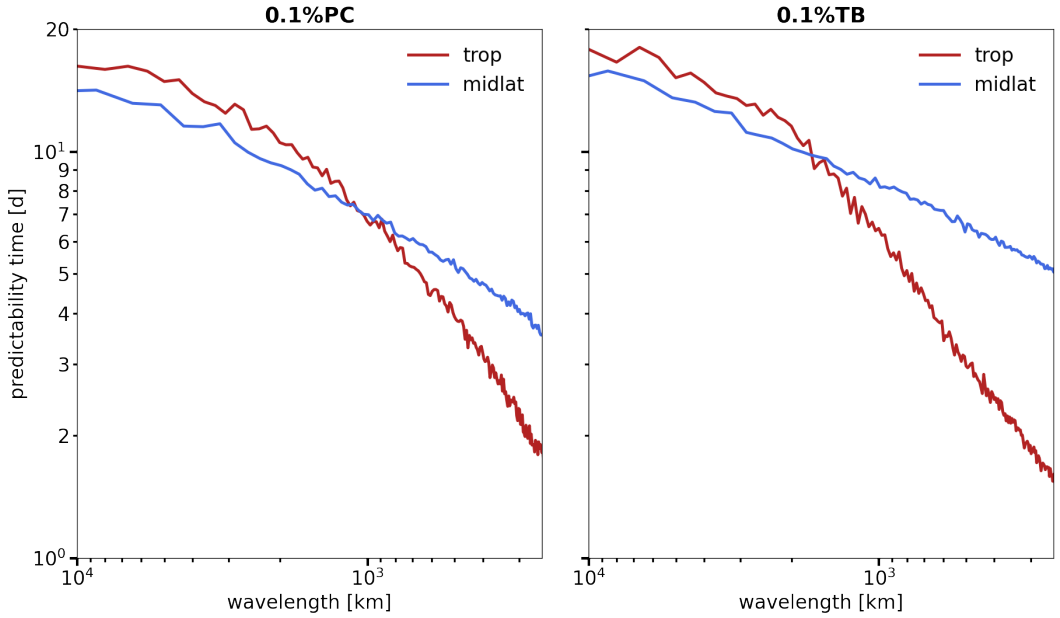

Figure 4.5: Predictability time over spatial scale (4.9 with $\alpha = 0.5$) for the 0.1%-experiments both for the PC and TB convection schemes for the tropics and mid-latitudes. Both axes are logarithmic.

For the small scales, below approximately 1000 and 2000 km for the PC and TB schemes, respectively, the predictability time limit is lower in the tropics and can be connected to the faster approach to saturation limits observed in the growth rate behavior (Fig. 4.4). However, for the large scales, the predictability times in the tropics become larger. Thus, on the small scale approximately 250 km, the predictability time limit estimates are about 1.8 and 3.5 days for the tropics and mid-latitudes, respectively, but on the large scale approximately 4000 km, the predictability time limit in the tropics is greater than in the mid-latitudes and equals 13.9 days (11.5 days in the mid-latitudes). In the mid-latitudes, the predictability time limit are longer for the TB convec-

tion scheme and can be associated with the overconfidence of the scheme. So, for the small scale about 250 km and for the large scale about 4000 km, the predictability time limits equal 5.0 and 13.2 days, respectively. In the tropics, on the small scales, the predictability time limit are shorter for the TB scheme due to the lower saturation limit and equals 1.6 days. On the large scales, the TB scheme shows longer predictability time estimations compared to the PC scheme, therefore the intersection of the predictability time curves occurs on the larger scales compared to the PC scheme. For the large scale about 4000 km, the predictability time limit for the TB scheme is equal to 14.8 days.

4.2 Error growth in spectral space

Since the simulation experiments of the previous chapters have shown the importance of spectral slope features behavior in connection with error propagation, this section is dedicated to the study of the spectral slope by 2D model for homogeneous turbulence in incompressible flow. The goal of this section is to explore the role of spectral slope in longer predictability time limit for the tropics on the base of the simple Lilly model.

In the first subsection, the basic theoretical concepts of the simple error propagation model proposed by Lilly (1972, 1990) are presented. The second subsection is devoted to the estimation of the error propagation times in the context of this model.

4.2.1 Simple Lilly model

The theoretical model of Lorenz (1969) describes homogeneous turbulence in 2D incompressible flow. Lorenz considers the background kinetic energy spectrum of the flow $E(k)$ proportional to a negative power law of the horizontal wavenumber k:

$$E(k) = Ak^{-m}, \tag{4.10}$$

where A is some flow constant. According to the model, an upscale cascade dominates in error growth and depends on the slope of $E(k)$ and the initial error. The initial errors on a small scale grow and mostly contaminate the adjacent larger scale in a logarithmic sense. The growth of eddies on this adjacent scale effects the next larger scale until the cascade reaches the largest scales.

To explain the dependence of error growth on the slope of $E(k)$, Lorenz (1969) and Lilly (1972) introduce a spectrally localized time constant $\tau(k)$, considered as proportional to the circulation time of eddies at that scale. Based on dimensional considerations, for each scale, an amplitude of a characteristic circulation velocity $v(k)$ is defined as $[kE(k)]^{1/2}$. Lorenz suggests that the time required for the initial errors localized on a scale k to grow and contaminate the larger scale $k/2$ is characterized by $\tau(k)$, with $\tau(k)$ is given as an inverse of circulation frequency:

$$\tau(k) = \frac{1}{kv(k)} = [k^3 E(k)]^{-\frac{1}{2}}. \tag{4.11}$$

Thus, the error propagation time from the small scale $2^N k$ to the large scale k is given by a sum $\sum_{n=0}^{N} \tau(2^n k)$ and is the timescale of predictability decay (Lilly, 1972). Taking into account (4.10), the equations (4.11) shows that time constant $\tau(k)$ does not depend on k for $m = 3$, which is a borderline case for predictability. For $m \geq 3$ an unlimited extension of predictability is possible by reducing the scale and amplitude of the initial errors. However, for $m < 3$, a complete loss of predictability for any nonzero initial error can be achieved in a finite time.

Lilly (1990) roughly generalized the Lorenz's result as an integral and received the total time required for the predictability at a large scale k_1 to be lost by the upscale growth of initial errors at a small scale k_0, given by

$$T = \int_{k_1}^{k_0} \tau(k) \mathrm{d}(\ln k) = \int_{k_1}^{k_0} [k^3 E(k)]^{-1/2} \mathrm{d}(\ln k), \tag{4.12}$$

considering the wavenumber spectrum as continuous. The equation (4.12) establishes a relationship between the predictability limit and the slope of background kinetic energy spectrum.

Thus, the Lilly model is only a simple model for the error propagation in the 2D homogeneous flow based on the upscale error growth cascade, dependent on the slope of the kinetic energy spectrum. However, for highly nonhomogeneous circulations, in which the error growth in physical space is strongly localized in the areas of moist convection, the error growth is not localized in spectral space due to the Fourier transform uncertainty principle. Therefore, the proposed successive scale-to-scale mechanism of error propagation can no longer be applied, since any scale is contaminated by the error growth from a range of different scales. Lloveras et. al. (2021) showed that, in consequence of that, the error spectra are almost insensitive to the scale of initial perturbation and slope of $E(k)$. It should be also noted that, according to atmospheric observations, the error propagation does not evolve successively scale-by-scale, but gradually increases on all scales.

4.2.2 Error propagation time estimation

In this subsection, an analytical experiment to explore the role of the spectral energy slope on the error propagation employing the Lilly model has been performed. As the input data for the Lilly model, the slopes evaluated for the tropics and mid-latitudes in subsection 4.1.2 have been applied, aiming to obtain:

- estimations for the error propagation times for the different spectral slopes;
- comparison error propagation times with the corresponding estimations obtained from the numerical simulations.

It should be noted that the Lilly model estimates the intrinsic limit of predictability and the simulations from the 0.1%PC-experiment were applied, which provides the closest estimations for the intrinsic predictability. The inertial range of the spectrum between the wavelengths of 400 and 4000 km, as

mentioned above, has been used by taking from the available spectral analysis scales the scales closest to these wavelengths.

Since the Lilly model is a simple model for predictability time estimation, for the current study, it was assumed to included an additional proportionality constant γ into (4.12):

$$T_L = \gamma \int_{k_1}^{k_0} [k^3 E(k)]^{-1/2} \mathrm{d}(\ln k). \tag{4.13}$$

Based on (4.10), $E(k)$ for some wavenumber k can be obtained as $E(k) = E_0(k/k_0)^{-m}$, where E_0 is the background KE at the wavenumber k_0. Substituting this expression into (4.13) and finding an analytical solution of the integral, the time for errors to propagate from the small scale k_0 to the large scale k_1 can be derived as

$$T_L = \begin{cases} \gamma \frac{2}{m-3} E_0^{-\frac{1}{2}} k_0^{-\frac{m}{2}} \left(k_0^{\frac{m-3}{2}} - k_1^{\frac{m-3}{2}} \right) & \text{for } m \neq 3, \\ \gamma E_0^{-\frac{1}{2}} k_0^{-\frac{3}{2}} \left(\ln k_0 - \ln k_1 \right) & \text{for } m = 3. \end{cases} \tag{4.14}$$

Thus, the error propagation time from the scale k_0 to the scale k_1 can be retrieved if the slope of energy spectrum m, background kinetic energy on the scale k_0 and the proportionality constant γ are known. On the other hand, from the equation (4.14), γ can be find as

$$\gamma = \begin{cases} \frac{m-3}{2} T_L E_0^{\frac{1}{2}} k_0^{\frac{m}{2}} \left(k_0^{\frac{m-3}{2}} - k_1^{\frac{m-3}{2}} \right)^{-1} & \text{for } m \neq 3, \\ T_L E_0^{\frac{1}{2}} k_0^{\frac{3}{2}} \left(\ln k_0 - \ln k_1 \right)^{-1} & \text{for } m = 3. \end{cases} \tag{4.15}$$

To perform estimations for the error propagation times for the different spectral slopes, the constant γ should be fixed and evaluated from (4.15) based on estimates from the numerical simulations, namely from the mid-latitude spectral analysis: the spectral slope $m_1 = 3.1$, kinetic energy E_0^{midlat} and the predictability time difference between the smallest and the largest scales $\Delta T^{midlat} = 6.8$ days (as T_L). The obtained proportionality constant is $\gamma = 5.3$. To assess the effect of the spectrum slope on the error propagation time, the estimation of the error propagation time for the slope $m_2 = 2.1$, obtained for the tropics from the spectral analysis, has been performed. As an initial assumption, it has been considered that on the small scale k_0 the values of E_0 are equal for different energy spectrum slopes (E_0-assumption). Substituting the constant γ and E_0^{midlat} into (4.14), the error propagation time between the smallest and the largest scales for the slope of m_2 has been estimated as a value of 12.2 days. Therefore, the obtained result shows that, according to the Lilly model, a shallower slope of the energy spectrum leads to longer predictability. For a comparison, the tropical predictability time difference ΔT^{trop} equals 10.7 days.

To compare error propagation times with the corresponding estimations obtained from the numerical simulations, the estimation described above has been performed for the whole inertial range both for the slopes of m_1 and m_2. Thus, the error propagation time from the nearest smaller scale k_0 to each scale k_i from the inertial range $T_L(k_i)$ has been evaluated from (4.14) substituting the constant γ and E_0^{midlat}. For the reference, from the numerical

simulation estimations the differences in the predictability time limits between each scale and the smallest scale have been determined. The obtained total error propagation times both for the tropics and mid-latitudes are presented in Fig. 4.6(a). As a result, the Lilly model, as well as the numerical simulations, provides longer predictability time limits for the tropics compared to the mid-latitudes over the considered spectrum range, therefore, longer predictability for a shallower slope of $E(k)$.

It should be noted, that the fact that, according to the Lilly model, a shallower slope of the background kinetic energy corresponds to longer predictability limit, is directly related to the spectral range, which has been investigated, and connected to the background kinetic energy levels on the investigated scales. Thus, if initially on small scales the background kinetic energy spectrum with a shallower slope has a higher energy level than the energy spectrum with a steeper slope, then with the increasing scale on a certain scale, the values of the energy levels will become equal and for the scales larger than the scale of intersection, the background kinetic energy spectrum with the shallower slope will have lower values than the spectrum with a steeper slope.

By E_0-assumption for the theoretical model, the background kinetic energy at the smallest scale is the same in the tropics and mid-latitudes. It should be noted, that the condition described above did not fit for the numerical simulations: E_0 in the mid-latitudes was approximately 2.7 times greater than in the tropics. As the second step of the investigation, a similar predictability assessment for $m = 2.1$ has been performed, this time taking into account the difference of E_0 for the two regions and considering $E_0^{trop} = E_0^{midlat}/R$, where R is a certain ratio. The obtained predictability estimations are also presented in Fig. 4.6(a) (dotted line) with $R = 2.7$ is taken from the numerical simulation results. In the case of taking into account the E_0 ratio the total error propagation time in the tropics is larger comparing with the assumption of equal E_0, but then total error propagation time estimation is less consistent with the numerical simulation estimations.

The last step of the investigation was the estimation of the error propagation time without explicit specification of the $E(k)$ slope by a numerical integration of (4.13). The background KE obtained from the spectral analysis has been used. Step by step, for each wavelength, the error propagation time from the nearest smaller scale k_0 to that scale k_i $\delta T_L^{int}(k_i)$ was evaluated as numerical integral between considered scales. Total error propagation time from the smallest scale to that scale $T_L^{int}(k_i)$ has been determined as the sum of the error propagation times for all smaller scales: $T_L^{int}(k_i) = \sum_{k=k_0}^{k_i} \delta T_L^{int}(k)$. The obtained estimations are shown on the Fig. 4.6(b). The total error propagation times for both parts of the analytical experiment are consistent with each other, which may confirm the accuracy of the spectral slope estimations performed in subsection 4.1.2.

The provided in the current study assessments show that for the Lilly model, in which the upscale cascade depending on the slope of $E(k)$ dominates in error growth, a shallower slope leads to longer predictability. Furthermore, the estimations for the total error propagation time showed that a shallower slope not only provides longer predictability but also the larger increase in the total error propagation time with increasing wavelength. The described behavior

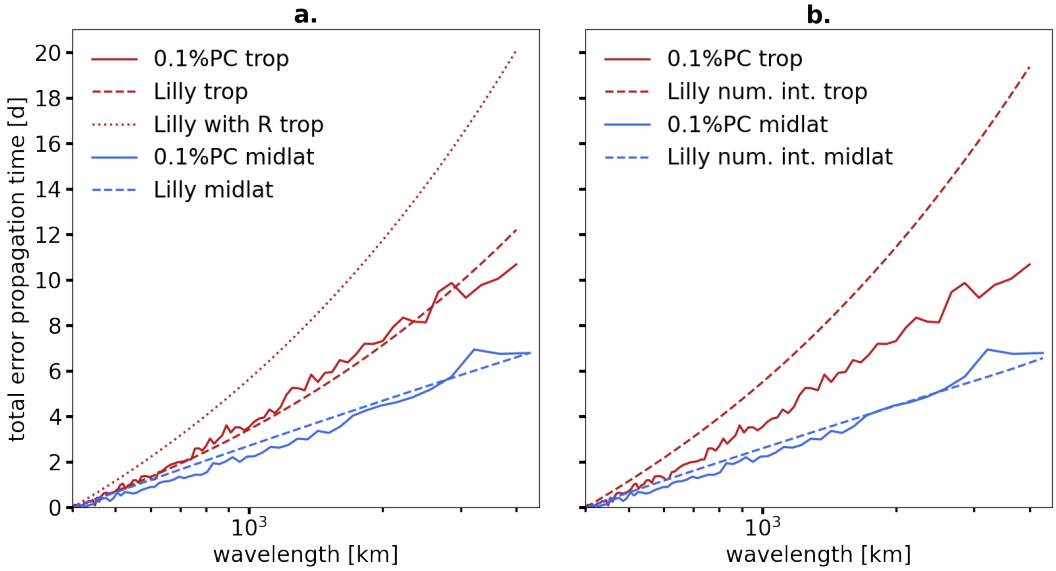

Figure 4.6: Total error propagation time estimations over spatial scale in the tropics and mid-latitudes estimated (a) based on the explicit spectral slope definition (4.14) and (b) by the numerical integration of (4.13). The horizontal axis is logarithmic. The solid lines show the 0.1%PC-experiment estimations. (a) The dashed red and blue lines are estimations for the Lilly model for $m = 2.1$ and $m = 3.1$, respectively. The dotted red line indicates the Lilly model estimations for the tropics with the E_0 ratio consideration. (b) The dashed lines are the Lilly model estimations based on numerical integration.

is characteristic both when the slope of $E(k)$ is specified and when $E(k)$ is substituted from the numerical model to the Lilly model. The same features appear in the estimations obtained from the spectral analysis of the numerical simulations.

Chapter 5

Summary and discussion

In the current study, the investigation of the tropical waves representation and estimation of the tropical predictability time limits in numerical simulations with the stochastic convection scheme were performed. Two primary objectives for the study were set. The first objective was the identification of the individual types of tropical waves in the meteorological fields: total precipitation, wind divergence and OLR. The second objective was the estimation of the practical and intrinsic limits of the predictability in the tropics and investigation of the transition between them. The important part of the study was the estimation of the intrinsic predictability limits in spectral space and the slope of the background kinetic energy spectrum. Previous studies (e.g. Ying and Zhang 2017; Judt 2020) have shown that tropical intrinsic predictability limits are longer compare to the extratropics, especially at large scales. The estimations of predictability time limits of the tropical waves have also shown their relatively long limits (Ying and Zhang 2017; Li and Stechmann 2020; Judt 2020), thus they may be associated with the longer tropical predictability limits. With that the spectral slope of the background kinetic energy may play a much more substantial role in the evolution of the error than the dynamics (Rotunno and Snyder 2008; Lilly 1972). Thus, the unifying aim of the current study was the examination of the hypothesis about the longer predictability limits in the tropics and consideration of the tropical waves and nature of the kinetic energy spectral slope as two possible sources of it.

To achieve the set objectives, the global numerical simulations on the base of ICON, conducted by Selz et al. (2022), were used. For the current study, the additional numerical simulations, also based on ICON, were performed for a longer model lead time and higher model resolution. In total, the study included eleven particular experiments: nine experiments of 31 days lead time on $\approx$ 40 km resolution and two additional experiments of 96 days lead time on $\approx$ 20 km resolution. All 31 days experiments contained 12 simulation cases each and were initialized from a broad range of initial condition uncertainty: from current estimates to reduced a thousand times to simulate the intrinsic predictability limits. The majority of the numerical simulations was performed for ICON with the stochastic convection scheme. The current study required the perfect model assumption for the intrinsic predictability limit estimation and applied the stochastic convection scheme to reduce the underestimation of upscale error growth from convection. Additionally, the simulations with the

deterministic convection scheme were used for the reference and comparison study.

The identification of the tropical waves was carried out on the basis of the time-longitude Hovmöller diagrams and Wheeler-Kiladis space-time analysis. For the comparison, the investigation was performed also for the numerical simulations with the deterministic convection scheme and the reanalysis data. On the Hovmöller diagrams for the total precipitation rate, a clear diurnal cycle and three longitudinal zones with strong convection activity are evidently visible, in line with tropical meteorology. In addition, zonally propagating systems with high precipitation intensity are notable, among which the specific tropical wave types can be recognized based on the propagation time, speed and direction. Thus, the wave patterns corresponding to ER and WIG waves were identified, which occur both in the stochastic numerical simulations and in the deterministic simulations and the reanalysis. However, the strength and character of these patterns differ for the PC scheme: patterns are very thin and distinct, with high precipitation concentration in contrast to more smooth and diffuse patterns for the TB scheme and ERA5. The significant difference between the numerical simulations with the stochastic scheme and two other data sources is the absence of Kelvin waves, which clearly occur in the TB and ERA5 diagrams, although are relatively weak, and are generally considered the most prominent and common type of CCEWs.

Further investigation of the tropical waves representation was performed by the means of the Wheeler-Kiladis space-time spectra diagnostic for the total precipitation rate, wind divergence (at 300, 200 and 100 hPa pressure level) and OLR. Consistent with the previous studies, the obtained spectra have a broad red nature, however, features superimposed upon the background spectrum can be recognized. Thus, on the Wheeler-Kiladis diagrams for total precipitation rate and OLR, a weak signals of Kelvin, ER and MRG waves are observed. Comparing the simulations with the stochastic and deterministic schemes, the wave signals are slightly weaker for the stochastic scheme. Furthermore, the simulations for both schemes show significantly weaker signals than the reanalysis and do not contain signs of WIG, appearing in the reanalysis and observed on the Hovmöller diagrams. However, the Wheeler-Kiladis diagrams for the wind divergence show a robust consistency between the convection schemes and the reanalysis for each investigated pressure levels. All three data sources obtain the signals of Kelvin, ER and MRG waves and the strength of these signals is similar among the sources, although the signals for the reanalysis are slightly stronger above the tropopause level (200 and 100 hPa). With the increasing altitude, the red nature of the spectra is less prominent and the signals of the tropical waves become clearer. However, the numerical simulations still show no prominent signals of WIG waves. Thereby, although the tropical waves are represented insufficiently in the total precipitation and OLR fields in the numerical simulation, robust wave signals can be identified in the wind divergence field. The obtained results may indicate that, although the tropical waves are represented in the numerical simulations with convection schemes, they are slightly coupled to the convection. Further, it can be assumed that the choice of the convection scheme affects the representation of coupling, since the tropical waves signals in total precipitation rate and OLR fields are weaker for

the stochastic scheme, although the signals in the wind divergence field show a similar strength. The misrepresentation of the CCEWs in current NWP models and reanalysis is known. Thus, comparison of the range of reanalyses on different model resolutions and with different convection schemes with observations show their significant deficiencies in representation of CCEWs (Kim and Alexander 2013).

The assessment of the predictability time limits in physical space in the numerical simulations with the stochastic convection scheme were performed for the range of the initial conditions perturbations, estimating the limit of current practical predictability, the limit very close to the intrinsic predictability limit and the transition between them. The estimations were performed both for the tropics and mid-latitudes to investigate the latitude dependence of the predictability time limits. The numerical simulations with the deterministic scheme were were also applied for the comparison. The obtained predictability time limits in the tropics are significantly longer than for the mid-latitudes for each range of the perturbations in the initial conditions. The intrinsic limit of predictability in the mid-latitudes is around two weeks and in the tropics this limit exceeds two weeks. Both estimations are consistent with many previous studies. A significant approach to the intrinsic limit of predictability can be achieved by 90% reduction of the initial conditions uncertainty, further uncertainty reduction will lead to relatively small improvement. The potential predictability improvement is larger in the tropics: 4-5 and 5-6 days for the mid-latitudes and tropics, respectively, depending on if singular vectors are included. Furthermore, predictability limis in the tropics show larger improvement for the same percentage of uncertainty reduction. However, since the accuracy of initial conditions in the tropics is currently improving more slowly compare to the mid-latitudes, it can be expected that it may take longer to reach the intrinsic predictability limit in the tropics. For the deterministic convection scheme the estimations of the predictability limit were longer compare to the stochastic scheme and this trend was more significant for the larger reduction of the initial condition uncertainty, thus the choice of the convection scheme may become significant with reducing uncertainty in the initial conditions.

The estimation of the intrinsic predictability limits was also performed in spectral space. For the small scales, the predictability time limits in the mid-latitude are longer compare to the tropics, however for the large scale the opposite is true, which is consistent with previous studies. The investigation of error growth based on spectral DKE show a fast downscale error propagation over first few hours and the error growth rate is significantly higher in the tropics especially on the small scales. Following few days, error growth slows down becoming lower in the tropics and upscale error propagation is observed. After this period, errors approach saturation limits on the small scale and up-magnitude behavior on the synoptic and planetary scales dominates, also noted in range of other studies. In the tropics the error saturation become faster, which together with the larger error growth during first few hours leads to relatively short predictability limits on the small scales. Thus, shorter predictability limits on the small scales in the tropics may be explained by impact of strong convective processes, while longer predictability on the large scales may potentially be associated with the tropical waves.

However, the assessment of the spectral slope of background kinetic energy in inertial range show a significant difference between the tropics and mid-latitudes. The obtained slope in the tropics is shallower than in the mid-latitudes (2.1 versus 3.1) and potentially may also affect the tropical predictability time limits. The investigation of the role of spectral slope in predictability limits was performed using the simple Lilly model, in which for error propagation time only the kinetic energy spectrum is considered. For the comparison, flows with two different spectral slopes were investigated and the slopes were chosen as the obtained in spectral analysis. It was assumed that the flows have the same background kinetic energy at the smallest scale of the investigated range to evaluate effect on error propagation time only of the different slope values. The Lilly model provides a longer predictability time limits for the shallower slope, which may indicate that the shallower tropical slope itself may lead to a longer predictability in the tropics. Further, little bit more realistic case were investigated assuming that the energy values at the smallest scale are related with the certain ratio, consistent with the numerical simulations. In this case, the predictability estimates for a shallower slope were even longer than previous Lilly estimations and estimations from the numerical simulations. It may indicate that the long predictability from the nature of the spectral slope may be reduced by the atmospheric processes presented in the numerical models, in contrast of simple theoretical model.

Summarizing all obtained results, the predictability time estimations provided, as was expected, longer tropical predictability, especially for the large scales. According to the identification of the tropical waves, although certain wave signals were recognized, the numerical simulations with the stochastic convection scheme are exposed a significant misrepresentation of tropical waves. The misrepresentation makes it difficult to estimate their effect on the tropical predictability. Further investigation is needed, which can consist of the separation of individual wave types based on filtering in wavenumber-frequency domain and estimation of their predictability limits. However, the investigation of the spectral slope role in longer predictability showed a significant sign that the shallower spectral slope may be a source of the longer predictability limits, but it should be taking into account that Lilly model is only a simple model of error propagation assumed the upscale error grown. Various model studies and atmospheric observations show rather up-magnitude error growth.

Bibliography

Bechtold, P., Köhler, M., Jung, T., Doblas-Reyes, F., Leutbecher, M., Rodwell, M. J., Vitart, F., and Balsamo, G.: Advances in simulating atmospheric variability with the ECMWF model: From synoptic to decadal time-scales, Quarterly Journal of the Royal Meteorological Society: A journal of the atmospheric sciences, applied meteorology and physical oceanography, 134, 1337–1351, doi:10.1002/qj.289, 2008.

Chang, C.-P.: Westward propagating cloud patterns in the tropical Pacific as seen from time-composite satellite photographs, Journal of Atmospheric Sciences, 27, 133–138, 1970.

Cohen, B. G. and Craig, G. C.: Fluctuations in an equilibrium convective ensemble. Part II: Numerical experiments, Journal of the atmospheric sciences, 63, 2005–2015, doi:10.1175/JAS3710.1, 2006.

Doms, G. and Schattler, U.: A description of the nonhydrostatic regional model LM, Part II: Physical Parameterization, Tech. rep., Deutscher Wetterdienst, 2004.

Durran, D., Weyn, J. A., and Menchaca, M. Q.: Practical considerations for computing dimensional spectra from gridded data, Monthly Weather Review, 145, 3901 – 3910, doi:10.1175/MWR-D-17-0056.1, 2017.

Durran, D. R. and Gingrich, M.: Atmospheric predictability: Why butterflies are not of practical importance, Journal of the Atmospheric Sciences, 71, 2476 – 2488, doi:10.1175/JAS-D-14-0007.1, 2014.

ECMWF: Annual Report 2017, European Centre for Medium-Range Weather Forecast, pp. 1–40, 2018.

Feeley, K. J. and Stroud, J. T.: Where on Earth are the "tropics"?, Frontiers of Biogeography, 10, doi:10.21425/F5FBG38649, 2018.

Gruber, A.: The wavenumber-frequency spectra of satellite-measured brightness in the tropics, Journal of Atmospheric Sciences, 31, 1675–1680, 1974.

Heise, E., Ritter, B., and Schrodin, E.: Operational implementation of the multilayer soil model TERRA, Tech. rep., Deutscher Wetterdienst, 2006.

Holton, J. R.: Waves in the equatorial stratosphere generated by tropospheric heat sources, Journal of Atmospheric Sciences, 29, 368–375, 1972.

Holton, J. R.: On the frequency distribution of atmospheric Kelvin waves, Journal of Atmospheric Sciences, 30, 499–501, 1973.

Holton, J. R. and Hakim, G. J.: An Introduction to Dynamic Meteorology, Academic Press, 2013.

Hung, M.-P., Lin, J.-L., Wang, W., Kim, D., Shinoda, T., and Weaver, S. J.: MJO and convectively coupled equatorial waves simulated by CMIP5 climate models, Journal of Climate, 26, 6185 – 6214, doi:10.1175/JCLI-D-12-00541.1, 2013.

Judt, F.: Insights into atmospheric predictability through global convection-permitting model simulations, Journal of the Atmospheric Sciences, 75, 1477 – 1497, doi:10.1175/JAS-D-17-0343.1, 2018.

Judt, F.: Atmospheric predictability of the tropics, middle latitudes, and polar regions explored through global storm-resolving simulations, Journal of the Atmospheric Sciences, 71, 257–276, doi:10.1175/JAS-D-19-0116.1, 2020.

Judt, F. and Rios-Berrios, R.: Resolved convection improves the representation of equatorial waves and tropical rainfall variability in a global nonhydrostatic model, Geophysical Research Letters, 48, e2021GL093 265, doi:10.1029/2021GL093265, 2021.

Kain, J. S. and Fritsch, J. M.: A one-dimensional entraining/detraining plume model and its application in convective parameterization, Journal of Atmospheric Sciences, 47, 2784–2802, doi:10.1175/1520-0469(1990)047, 1990.

Keane, R. and Plant, R.: Large-scale length and time-scales for use with stochastic convective parametrization, Quarterly Journal of the Royal Meteorological Society, 138, 1150–1164, doi:10.1002/qj.992, 2012.

Keane, R. J., Craig, G. C., Keil, C., and Zängl, G.: The Plant–Craig stochastic convection scheme in ICON and its scale adaptivity, Journal of the Atmospheric Sciences, 71, 3404–3415, doi:10.1175/JAS-D-13-0331.1, 2014.

Kiladis, G. N., Wheeler, M. C., Haertel, P. T., Straub, K. H., and Roundy, P. E.: Convectively coupled equatorial waves, Reviews of Geophysics, 47, doi:10.1029/2008RG000266, 2009.

Kim, J.-E. and Alexander, M.: Tropical precipitation variability and convectively coupled equatorial waves on submonthly time scales in reanalyses and TRMM, Journal of Climate, 26, 3013–3030, doi:10.1175/JCLI-D-12-00353.1, 2013.

Li, Y. and Stechmann, S. N.: Predictability of tropical rainfall and waves: Estimates from observational data, Quarterly Journal of the Royal Meteorological Society, 146, 1668–1684, doi:10.1002/qj.3759, 2020.

Lilly, D. K.: Numerical simulation studies of two-dimensional turbulence: II. Stability and predictability studies, Geophysical Fluid Dynamics, 4, 1–28, 1972.

Lilly, D. K.: Numerical prediction of thunderstorms – has its time come?, Quarterly Journal of the Royal Meteorological Society, 116, 779–798, doi: https://doi.org/10.1002/qj.49711649402, 1990.

Lin, J.-L., Kiladis, G., Mapes, B., Weickmann, K., Sperber, K., Lin, W., Wheeler, M., Schubert, S., Genio, D., Donner, L., Emori, S., Gueremy, J.-F., Hourdin, F., Rasch, P., Roeckner, E., and Scinocca, J.: Tropical intraseasonal variability in 14 IPCC AR4 climate models. Part I: Convective signals, J. Climate, 19, 2665–2290, doi:10.1175/JCLI3735.1, 2006.

Lloveras, D. J., Tierney, L. H., and Durran, D. R.: Mesoscale predictability in moist midlatitude cyclones is not sensitive to the slope of the background kinetic energy spectrum, Journal of the Atmospheric Sciences, 79, 119 – 139, doi:10.1175/JAS-D-21-0147.1, 2022.

Lorenz, E. N.: The predictability of a flow which possesses many scales of motion, Tellus, 21, 289–307, doi:10.1111/j.2153-3490.1969.tb00444.x, 1969.

Lott, F. and Miller, M. J.: A new subgrid-scale orographic drag parametrization: Its formulation and testing, Quarterly Journal of the Royal Meteorological Society, 123, 101–127, 1997.

Madden, R. A. and Julian, P. R.: Observations of the 40–50-day tropical oscillation – a review, Monthly Weather Review, 122, 814 – 837, doi:10.1175/1520-0493(1994)122, 1994.

Maruyama, T.: Large-scale disturbances in the equatorial lower stratosphere, Journal of the Meteorological Society of Japan. Ser. II, 45, 391–408, 1967.

Matsuno, T.: Quasi-geostrophic motions in the equatorial area, Journal of the Meteorological Society of Japan. Ser. II, 44, 25–43, doi: 10.2151/jmsj1965.44.1_25, 1966.

Mlawer, E. J., Taubman, S. J., Brown, P. D., Iacono, M. J., and Clough, S. A.: Radiative transfer for inhomogeneous atmospheres: RRTM, a validated correlated-k model for the longwave, Journal of Geophysical Research: Atmospheres, 102, 16 663–16 682, 1997.

Nastrom, G., Gage, K., and Jasperson, W.: Kinetic energy spectrum of large- and mesoscale atmospheric processes, Nature, 310, 36–38, 1984.

Orr, D. M., Burrows, W. H., Hendricksen, R. E., Clem, R. L., Back, P. V., Rutherford, M. T., Myles, D. J., and Conway, M. J.: Impacts of grazing management options on pasture and animal productivity in a Heteropogon contortus (black speargrass) pasture in central Queensland. 1. Pasture yield and composition, Crop and Pasture Science, 61, 170–181, 2010.

Plant, R. S. and Craig, G. C.: A tochastic parameterization for deep convection based on equilibrium statistics, Journal of the Atmospheric Sciences, 65, 87–105, doi:10.1175/2007JAS2263.1, 2008.

Raschendorfer, M.: The new turbulence parameterization of LM, COSMO newsletter, 1, 89–97, 2001.

Reed, R. J. and Recker, E. E.: Structure and properties of synoptic-scale wave disturbances in the equatorial western Pacific, Journal of the Atmospheric Sciences, 28, 1117–1133, 1971.

Riehl, H.: Climate and Weather in the Tropics, Academic Press, 1979.

Rotunno, R. and Snyder, C.: A generalization of Lorenz's model for the predictability of flows with many scales of motion, Journal of the Atmospheric Sciences, 65, 1063 – 1076, doi:10.1175/2007JAS2449.1, 2008.

Roundy, P. E. and Frank, W. M.: A climatology of waves in the equatorial region, Journal of the Atmospheric Sciences, 61, 2105 – 2132, doi:10.1175/1520-0469(2004)061, 2004.

Seifert, A.: A revised cloud microphysical parameterization for COSMO-LME, COSMO Newsletter, 7, 25–28, 2008.

Selz, T.: Estimating the intrinsic limit of predictability using a stochastic convection scheme, Journal of the Atmospheric Sciences, 76, 757 – 765, doi: 10.1175/JAS-D-17-0373.1, 2019.

Selz, T. and Craig, G. C.: Simulation of upscale error growth with a stochastic convection scheme, Geophysical Research Letters, 42, 3056–3062, doi: 10.1002/2015GL063525, 2015a.

Selz, T. and Craig, G. C.: Upscale error growth in a high-resolution simulation of a summertime weather event over Europe, Monthly Weather Review, 143, 813–827, doi:10.1175/MWR-D-14-00140.1, 2015b.

Selz, T., Riemer, M., and Craig, G. C.: The transition from practical to intrinsic predictability of midlatitude weather, Journal of the Atmospheric Sciences, doi:10.1175/JAS-D-21-0271.1, 2022.

Smith, R. K.: Lectures on Tropical Meteorology, Ludwig-Maximilians-Universität München – Meteorologisches Institut, 2003.

Sobel, A. H.: Tropical weather, Nature Education Knowledge, 3, 2, 2012.

Takayabu, Y. N.: Large-scale cloud disturbances associated with equatorial waves Part I: Spectral features of the cloud disturbances, Journal of the Meteorological Society of Japan. Ser. II, 72, 433–449, 1994.

Tiedtke, M.: A comprehensive mass flux scheme for cumulus parameterization in large-scale models, Monthly Weather Review, 117, 1779–1800, doi: 10.1175/1520-0493(1989)117, 1989.

Vallis, G. K.: Atmospheric and Oceanic Fluid Dynamics, Cambridge University Press, 2017.

Vogel, P., Knippertz, P., Fink, A. H., Schlueter, A., and Gneiting, T.: Skill of global raw and postprocessed ensemble predictions of rainfall in the tropics, Weather and Forecasting, 35, 2367–2385, doi:10.1175/WAF-D-20-0082.1, 2020.

Wallace, J. and Chang, L.: On the application of satellite data on cloud brightness to the study of tropical wave disturbances, Journal of the Atmospheric Sciences, 29, 1400–1403, 1972.

Wallace, J. M. and Kousky, V.: Observational evidence of Kelvin waves in the tropical stratosphere, Journal of Atmospheric Sciences, 25, 900–907, 1968.

Wheeler, M.: Tropical Meteorology: Equatorial Waves, in: Encyclopedia of Atmospheric Sciences, edited by Holton, J. R., pp. 2313–2325, Academic Press, Oxford, doi:10.1016/B0-12-227090-8/00414-0, 2003.

Wheeler, M. and Kiladis, G. N.: Convectively coupled equatorial waves: analysis of clouds and temperature in the wavenumber–frequency domain, Journal of the Atmospheric Sciences, 56, 374–399, doi:10.1175/1520-0469(1999)056, 1999.

Wheeler, M. and Nguyen, H.: Tropical Meteorology: Equatorial Waves, 2015.

Yanai, M. and Maruyama, T.: Stratospheric wave disturbances propagating over the equatorial Pacific, Journal of the Meteorological Society of Japan. Ser. II, 44, 291–294, 1966.

Ying, Y. and Zhang, F.: Practical and intrinsic predictability of multiscale weather and convectively coupled equatorial waves during the active phase of an MJO, Journal of the Atmospheric Sciences, 74, 3771–3785, doi:10.1175/JAS-D-17-0157.1, 2017.

Zangvil, A.: Temporal and spatial behavior of large-scale disturbances in tropical cloudiness deduced from satellite brightness data, Monthly Weather Review, 103, 904–920, 1975.

Zangvil, A. and Yanai, M.: Upper tropospheric waves in the tropics. Part I: Dynamical analysis in the wavenumber-frequency domain, Journal of the Atmospheric Sciences, 37, 283–298, 1980.

Zangvil, A. and Yanai, M.: Upper tropospheric waves in the tropics. Part II. Association with clouds in the wavenumber-frequency domain, Journal of Atmospheric Sciences, 38, 939–953, 1981.

Zhang, F., Sun, Y. Q., Magnusson, L., Buizza, R., Lin, S.-J., Chen, J.-H., and Emanuel, K.: What is the predictability limit of midlatitude weather?, Journal of the Atmospheric Sciences, 76, 1077–1091, doi:10.1175/JAS-D-18-0269.1, 2019.

Zhu, H., Wheeler, M. C., Sobel, A. H., and Hudson, D.: Seamless precipitation prediction skill in the tropics and extratropics from a global model, Monthly Weather Review, 142, 1556–1569, doi:10.1175/MWR-D-13-00222.1, 2014.

Zängl, G., Reinert, D., Rípodas, P., and Baldauf, M.: The ICON (ICOsahedral Non-hydrostatic) modelling framework of DWD and MPI-M: Description of the non-hydrostatic dynamical core, Quarterly Journal of the Royal Meteorological Society, 141, 563–579, doi:10.1002/qj.2378, 2015.

Acknowledgements

First, I would like to thank Prof. George Craig and Dr. Tobias Selz for giving me the opportunity to write this thesis. I especially would like to thank Dr. Tobias Selz for his time, advices and understanding, and for patiently answering all the questions that I had. And also I would like to thank Prof. George Craig for the Advanced Atmospheric Dynamics 2 course, where a lot of interesting and useful for my thesis papers were covered.

Next, I would like to thank Dr. Robert Redl for Python knowledgments I get during my HiWi-job, which were also useful for my thesis. Furthermore, I would like to thank all the W2W community for very friendly and supportive atmosphere.

Moreover, I would like to thank my friends and family for love and support during this year. I especially would like to thank my friend Ilya for his given advices and ideas. I also would like to thank my partner Kanstantsin for his emotional and technical support.

Declaration

I hereby declare that this thesis is my own work, and that I have not used any sources and aids other than those stated in the thesis.

Munich, 22. June 2022 Tatsiana Bardachova